2015

Heat Transfer Study of Porous Media with a Temperature Jump Condition

Pravin Kumar
Louisiana State University and Agricultural and Mechanical College, pravin.gangwar@gmail.com

HEAT TRANSFER STUDY OF POROUS MEDIA WITH A TEMPERATURE JUMP CONDITION

A Thesis

Submitted to the Graduate Faculty of the
Louisiana State University and Agricultural and Mechanical College
in partial fulfillment of the
requirements for the degree of
Master of Science

in

The Department of Mechanical and Industrial Engineering

by
Pravin Kumar
B. Tech, Indian Institute of Technology Kanpur, 2009
December 2015

Acknowledgments

I would like to thank Dr. Michael J. Martin for providing me this opportunity to carry out my research. I will always be grateful for his invaluable guidance and support during my entire graduate program at LSU. I can never repay for his efforts to show me the right path whenever I needed most and for always supporting me financially and emotionally. I am glad to be one of his student. I would also like to thank Dr. Ingmar Schoegl, Dr. Ram Devireddy and Dr. Patrick Mensah for serving on my advisory committee and for their invaluable time and thoughtful comments on my thesis. I am also thankful to Dr. Michael Pauken for making this research opportunity available, without his support the foundation would never be possible.

I would like to thank my friends for wonderful times I had during my stay at LSU. They were always there whenever I needed them most. They always stood by my side for emotional support when I missed my family across the globe. They also distracted me enough to keep me off the desk to freshen my mood whenever I needed. For this I thank, Ajay, Abhilash, Anton, Padmapriya, Mohan, Tathagat, and Manoj. I specially thank Anton since he was like a brother to me. Unfortunately, he is no more but I can never forget him for always being there for me.

I would like to thank Louisiana Space Grant Consortium (LaSPACE) and Department of Mechanical and Industrial Engineering for supporting me financially throughout my graduate studies. I also thank Louisiana Optical Network Initiative (LONI) for providing me resources to carry out my research.

Finally I would like to thank to my wife Swati for her support, encouragement and being a part of my journey. I am also thankful to my parents, Manoj and Arti for their support.

Table of Contents

List of Symbols

C	Constant
C_p	Specific heat (J/kg-K)
d_m	Collision diameter (m)
f	Frequency (Hz)
J	Jacobian
k	Thermal conductivity (W/m-K)
k_B	Boltzmann constant
k_g	Thermal conductivity of Gas (W/m-K)
K_{nL}	Knudsen number based on length
k_s	Thermal conductivity of Solid (W/m-K)
L	Length (m)
L_g	Characteristic length of the cavity (m)
L_s	Length of the solid
n	Wall-normal coordinate
P	Pressure (Pa)
P_r	Prandtl number
q''	Heat Flux (W/m^2)
q''_c	Heat Flux in continuum regime (W/m^2)
$\dot{q}_{in}$	Incoming Heat Flux rate (W/m^2s)
q''_o	Amplitude of heat flux in unsteady state (W/m^2)
$\dot{q}_{out}$	Outgoing Heat Flux rate (W/m^2s)
q''_x	Heat Flux in x direction
Q	Total Heat (W/m)
R	Thermal Resistance (K-m/W)
R_{eff}	Effective Thermal Resistance (K-m/W)
t	Time (s)
T	Temperature (K)
T_b	Boundary Temperature(K)
T_g	Gas temperature (K)
T_o	Reference Temperature(K)
T_w	Wall temperature (K)
T_x	Temperature Gradient in x direction
T_y	Temperature Gradient in y direction
T_ξ	Temperature gradient in ξ direction
T_η	Temperature gradient in η direction
$T_{\xi\xi}$	Temperature derivative in ξ direction
$T_{\eta\eta}$	Temperature derivative in η direction

x	Length-wise coordinate (m)
x_ξ	Position derivative in ξ direction
$x_{\xi\xi}$	Position derivative in ξ direction
$y_{\eta\eta}$	Position derivative in η direction
y_η	Position derivative in η direction
y	Length-wise coordinate (m)
α	Thermal diffusivity (m^2/s)
Δ	Step size
η	Non-dimensional position
γ	Specific heat ratio
μ	Viscosity(Pa.s)
λ	Mean free path (m)
ρ	Density (kg/m^3)
σ_T	Thermal accommodation coefficient
τ	Non-dimensional time
θ	Non-dimensional temperature
θ_g	Non-dimensional gas temperature
θ_w	Non-dimensional wall temperature
ω	Angular frequency (s^{-1})
ξ	Non-dimensional position

Abstract

Conjugate heat transfer in a porous media is investigated with a temperature jump condition obtained from kinetic gas theory. The temperature jump appears alongside flow boundary condition when the pressure is low, and considered to be in non-continuum regime. This investigation focuses on both one-dimensional and two-dimensional porous media models. The length scale of the pores is 100 microns. The temperature is ambient, and the pressure is low enough to reach the slip-flow regime.

The thermal behavior of porous media is investigated using a slot model with a gas trapped between two solid blocks. Aluminum oxide and air are considered as a baseline combination. The steady-state results show the change in the temperature jump and net heat flux as a function of Knudsen number for gas-solid systems. For unsteady cases, a change in the amplitude and phase of the heat flux is shown over the range of frequencies between 10 Hz and 10 kHz. The effects of different solid-gas combinations are also investigated. The results show that the properties of the gas has a significantly larger impact than those of the solid.

Steady-state heat transfer in two-dimensional porous media is also investigated using a brick model with a rectangular cavity of 90% void fraction. The results show the effects of pressure, void fraction and solid-gas combinations on the effective thermal conductivity of the porous media model. A multi-cell structure is also investigated to study the effective thermal conductivity and edge effects when low number of cells are considered. Pressure dependent thermal properties of the gases and silica based solid non-porous materials are also investigated due to their very low thermal conductivity.

Chapter 1 . Introduction

The pressure-dependent behavior of porous insulation in gas has been a topic of considerable controversy. Previous researchers investigated various types of porous insulators such as carbon foams (Druma, 2004), fiber thermal insulations (Petrov, 1997), porous ceramic materials (Litovsky, 1992 and Litovsky, 1996). Their investigations demonstrated the dependence of effective thermal conductivity on variables such as the gas present in pores, pressure, temperature, pore size, and porosity (Pauken, 2011) (Du, 2008). Pauken, et al. demonstrated at high temperatures and pressures, similar to those that may be encountered in future Venus missions, the thermal conductivity of the porous insulations, depends on the pressure of the gas (Figure 1.1). This suggests the need of further investigations to understand thermal behavior of the porous materials.

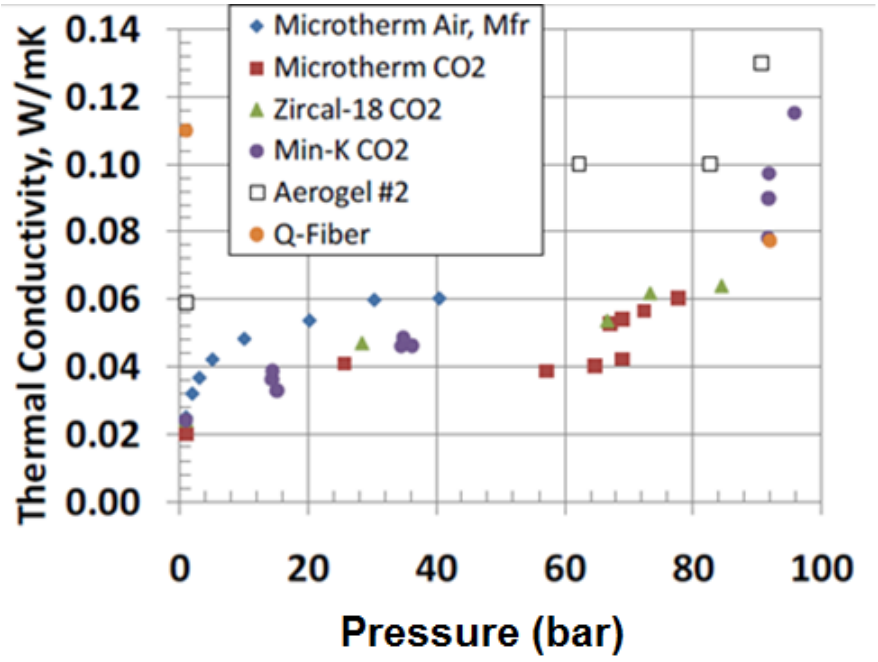

Figure 1.1. Thermal conductivity and pressure test results (Pauken, 2011)

Calculating the effective thermal conductivity and thermal response of a porous material requires taking into account the properties of both the gas and the solid, and any interfacial

resistance between the two phases (Smoluchowski, 1898). Druma, et al. demonstrated the complexity of determining effective thermal conductivity in carbon foam and its dependence on porosity of the material defined as volume fraction of cavities. Previous studies suggests that the effective thermal conductivity of porous ceramic materials depends highly on the gas pressure and temperature (Pauken, 2011 and Nutsugah, 2014). At high temperatures, the effective thermal conductivity of porous ceramic materials is governed by a thermal radiation model. At high pressures, it is governed by free convective gas motion (Litovsky, 1992 and Litovsky, 1996). However, at low pressures where gas falls into non-continuum regime, the thermal conductivity is governed by the Knudsen number. The Knudsen is the ratio of the mean free path λ, the distance traveled by the gas molecule before subsequent collisions and the characteristic length L:

$$Kn_L = \frac{\lambda}{L}. \tag{1.1}$$

where Kn_L is the Knudsen number, λ is mean free path, and L is characteristic length. The mean free path of the gas is the distance the gas molecule travels before it collides with another gas molecule, and is given by:

$$\lambda = \frac{k_b \cdot T}{\sqrt{2} \cdot \pi \cdot {d_m}^2 \cdot P} \tag{1.2}$$

where k_b is the Boltzmann constant, P is the pressure, and d_m is the diameter of the molecule. The value of d_m for the air, carbon dioxide, and hydrogen, as well as all other gas properties used in this investigation, are given in Chapter 2.

For Knudsen numbers of less than 0.001, the gas is considered a continuum, where the Navier-Stokes equations and Fourier energy transport model with no slip wall condition or temperature jump are valid. For Knudsen numbers between 0.001 and 0.1, the gas is in the slip flow regime, where velocity and temperature jump boundary conditions are used for the momentum and energy

conservation equations. For a Knudsen number between 0.1 and 10, the gas in in the transition flow regime, where the effect of collisions must be considered, but the collisions are not frequent enough to satisfy the continuum assumption. For Knudsen numbers greater than 10, the flow is free-molecular flow because of negligible molecular interactions (Park, 2002).

In many porous materials, the length scales of the pores puts the system in the slip-flow regime. Hence velocity and temperature jump conditions must be considered for solid-gas interaction near wall. These conditions can be found from the kinetic theory. The current work seeks to quantify the effects of the Knudsen number on unsteady heat transfer in porous materials. This numerical study will provide fundamental understanding of thermal behavior at micro scale level.

Firouzi, et al. demonstrated effects of wall-molecular interaction on mass transport using one-dimensional porous media slot model. A similar slot model can be used to investigate the thermal behavior of the porous media as the Knudsen number of the gas in the cavity falls in the slip flow regime as pressure of the gas decreases, shown further in this thesis for the slot size of 100 microns. To incorporate the effects of slip flow regime on conduction heat transfer, energy conservation equation must be solved with a temperature jump boundary condition (Smoluchowski, 1898) which can be found from kinetic theory:

$$T_{gas} - T_w = \frac{\lambda}{\Pr}\frac{2-\sigma_T}{\sigma_T}\frac{2\gamma}{\gamma+1}\left.\frac{\partial T}{\partial n}\right|_{wall} \tag{1.3}$$

where T_g is the gas temperature, T_w is the wall temperature, λ is the mean free path of the gas, γ is the specific heat ratio of the gas, Pr is the Prantdl number of the gas, σ_T is the thermal accommodation coefficient, and $\partial T/\partial n$ is the normal temperature gradient.

For heat transfer between the solid and gas portion of a porous media, the length scale of the gradient will be the size of the gap L. Using the non-dimensional co-ordinate n^* equal to n/L, equation (1.3) becomes:

$$T_{gas} - T_w = Kn_L \cdot C \cdot \left. \frac{\partial T}{\partial n^*} \right|_{wall} \tag{1.4}$$

where Kn_L is the Knudsen number for the system. C will be a function of the gas and surface properties:

$$C = \frac{2-\sigma_T}{\sigma_T} \cdot \frac{1}{\Pr} \cdot \frac{2\gamma}{\gamma+1}. \tag{1.5}$$

The definition of Knudsen number, and the commonly-used formula for mean free path, show that the Knudsen number and temperature jump will decrease as the pressure increases:

$$Kn_L = \frac{\lambda}{L}, \tag{1.1}$$

$$\lambda = \frac{k_b \cdot T}{\sqrt{2} \cdot \pi \cdot {d_m}^2 \cdot P}. \tag{1.2}$$

These equations show a possible mechanism for the pressure-dependent thermal conductivity of porous materials. At atmospheric pressure, the pore sizes are small enough that the Knudsen number based on pore size is large enough to create a temperature jump. This increases the thermal resistance of the system. As the pressure increases, the mean free path and the Knudsen number decrease, causing the temperature jump to disappear. This leads to decreased resistance, and a higher thermal conductivity.

The results of this study will further allow the understanding of the effects of gases permeating the insulation used in thermal protection systems used in Venus missions. Previous studies suggest that Venus possess one of the most hostile environments among proposed planetary exploration targets (Basilevsky, 2007). Pauken, et al., studied several insulation materials with simulated Venus-like conditions, showing pressure-dependent materials properties. This study will also be useful for similar problems encountered in high pressure systems such as deep-water operations (Zheng, 2001 and Woodside, 2003) and carbon sequestration (Gunter, 2002).

The temperature jump equation (1.4) discussed in this chapter will be considered for further investigation of the effects of pressure, Knudsen number, solid and gas thermal properties, size of the pore etc. Chapter 2 focuses on a one-dimensional slot model of the porous media and presents the results for steady state and unsteady state heat transfer. Chapter 3 focuses on the two-dimensional rectangular cavity to study steady state heat transfer as well as effective thermal conductivity of multiple pores stacked in series.

Chapter 2 . Unsteady Heat Transfer in One-Dimensional Slot Model

2.1. Introduction

Steady-state and unsteady heat transfer in one-dimensional slot model of the porous media is investigated in slip flow regime. This study begins by presenting the physical model used for this investigation with a cavity of the order of 100 micrometers surrounded by solid blocks. As discussed in the previous chapter, the temperature jump condition obtained from the kinetic gas theory is used at the solid-gas interface. The slot model is solved using the one-dimensional heat equation in conjunction with the temperature jump equations. The section will present the findings of one-dimensional unsteady and steady state heat transfer following by the discussion of the effects of the Knudsen number, gases and solids on the temperature jump and heat flux at the solid gas interface.

2.2. Physical Model

The porous media model is simplified with a one-dimensional slot model. Figure 2.1 represents a one-dimensional schematic diagram of one pore of the porous media. The cavity is filled with a gas, surrounded by the solids. The left side boundary is at a constant temperature, and the right side boundary is periodic temperature fluctuations with a finite amplitude. The solid phase has a thermal conductivity k_s, a density ρ_s, and a specific heat $c_{p,s}$. The gas phase has a thermal conductivity k_g, a density ρ_g, and a specific heat $c_{p,g}$. The difference in thermal properties of the solid and the gas results a discontinuity in the temperature gradient. However, a temperature jump also appear when the pressure of the gas is decreases such that the Knudsen number falls in the slip flow regime.

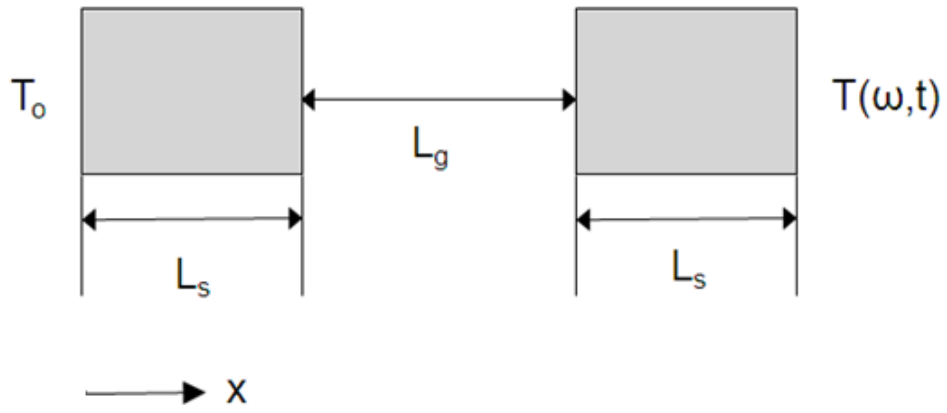

Figure 2.1 Schematic diagram of 1D slot model of porous media

For the given problem the one-dimensional heat equation can be solved using finite difference method and explicit scheme (Jaluria, 2002). The dimensional governing equations are defined as:

$$\frac{\partial T}{\partial t} = \alpha \frac{\partial^2 T}{\partial x^2}, \tag{2.1}$$

$$\alpha = \frac{k}{\rho c_p}, \tag{2.2}$$

$$T_{gas} - T_w = Kn_L \cdot C \cdot \left.\frac{\partial T}{\partial n^*}\right|_{wall}, \tag{1.4}$$

$$C = \frac{2-\sigma_T}{\sigma_T} \cdot \frac{1}{\Pr} \cdot \frac{2\gamma}{\gamma+1}, \tag{1.5}$$

$$Pr = \frac{\mu c_p}{k} \tag{2.3}$$

where T is the temperature, x is the position, t is the time, α is the thermal diffusivity, n^* is the normal direction to the wall, σ_T is the thermal accommodation coefficient, γ is the specific heat ratio, μ is the viscosity and P_r is the Prandtl number.

The non-dimensional governing equations are defined using non-dimensional temperature θ, non-dimensional position ξ and non-dimensional time τ.

$$\theta = \frac{T - T_o}{T_b - T_o}, \tag{2.4}$$

$$\xi = \frac{x}{L_g}, \tag{2.5}$$

$$\tau = \frac{\alpha t}{L_g^2}, \tag{2.6}$$

$$\frac{\partial \theta}{\partial \tau} = \frac{\partial^2 \theta}{\partial \xi^2}, \tag{2.7}$$

$$\theta_{gas} - \theta_w = Kn_L \cdot C \cdot \left.\frac{\partial \theta}{\partial n^*}\right|_{wall}. \tag{2.8}$$

These equations can be solved, using a finite-difference method that tracks both the wall and gas temperatures at the interface.

2.3. Computational Model

The equations are solved using one-dimensional slot model of porous media with explicit scheme of finite difference method. At the solid gas interface, the temperature jump equations is solved simultaneously with energy balance equation for both steady and transient case.

Figure 2.2a represents the discretization scheme for the governing heat equation (2.7) using an explicit scheme. Figure 2.2b represents a discretization scheme for the temperature jump condition at solid-gas interface based on equation (2.8).

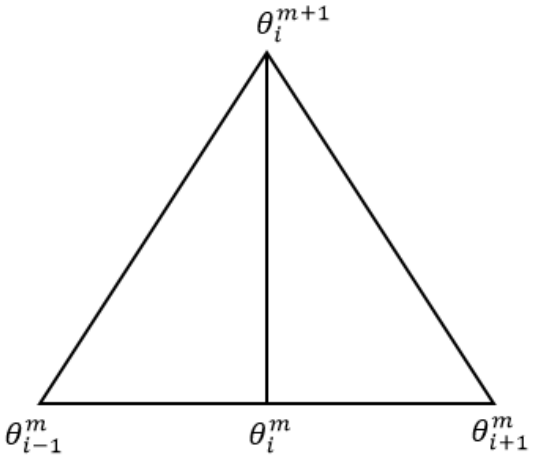

Figure 2.2a. Discretization scheme for one-dimensional heat equation

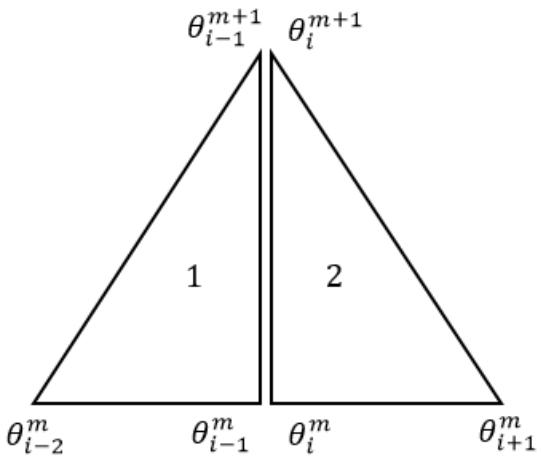

Figure 2.2b. Discretization scheme for solid-gas interface boundary

All the variables are known in previous time step '*m'*. Therefore, using a central difference method, the equation (2.7) at the time step '*m+1*':

$$\theta_i^{m+1} = \theta_i^m + \left(\frac{\theta_{i+1}^m - 2\theta_i^m + \theta_{i-1}^m}{(\Delta\xi)^2} \right) \Delta\tau \,. \tag{2.9}$$

where θ is the non-dimensional temperature, the subscript '*i*' is the position in *x* direction, the superscript '*m*' is the step, $\Delta\xi$ is the spatial step size and $\Delta\tau$ is the time step.

At the interface, a more complex discretization scheme is required for the wall discontinuity. This can be done by balancing the incoming and outgoing heat flux and energy accumulation:

$$\dot{q}_{in} + \dot{q}_{out} = \overline{\rho c_p} \cdot \left(\frac{\Delta T}{\Delta t} \right). \tag{2.10}$$

The discretization scheme for the conduction term will be:

$$\theta_i^{m+1} = \theta_i^m + \frac{\Delta\tau}{\overline{\Delta\xi}\,\overline{k}} \left(k_2 \frac{\theta_{i+1}^m - \theta_{i-1}^m}{\Delta\xi_2} - k_1 \frac{\theta_{i-1}^m - \theta_{i-2}^m}{\Delta\xi_1} \right), \tag{2.11}$$

$$\overline{\rho c_p} = \frac{\rho_1 c_{p,1} + \rho_2 c_{p,2}}{2}, \tag{2.12}$$

$$\overline{\Delta\xi} = \frac{\Delta\xi_1 + \Delta\xi_2}{2}, \tag{2.13}$$

$$\bar{k} = \frac{k_1 + k_2}{2}. \tag{2.14}$$

The discretization for temperature jump equation (2.8) will be:

$$\theta_{i-1}^{m+1} = \theta_i^{m+1} - Kn_L C \frac{L_2}{L_g}\left(\frac{\theta_{i+1}^m - \theta_i^m}{\Delta\xi_2}\right) \tag{2.15}$$

where the subscripts *'1'* and *'2'* refers to materials which can be either gas or solid depending upon left or right hand approach. $\Delta\xi$ is the distance between two nodes and $\Delta\tau$ is the size of time steps.

2.4. Physical Properties and Boundary Conditions

This investigation will cover several combinations of solids and gases, especially those widely adopted for aerospace applications. This section of the chapter focuses on Al_2O_3 as solid and Air as gas to study the effects of Knudsen number. Later part of the section will investigate the effects of the gases and solids for a fixed Knudsen number.

Table 2.1 gives the ideal gas constant R, thermal conductivity k_g, viscosity μ, specific heat ratio γ, specific heat c_p, Prandtl number Pr, and molecular diameter d_m of the gases used in this investigation (Bird, 1994, Xu 2003 and Tanaka, 1998).

Table 2.1. Gas Properties

Property	**Carbon Dioxide**	**Hydrogen**	**Air**
R (J/kg-K)	188.9	4124	286.9
k_g (W/m-K)	0.0146	0.1805	0.0243
μ (kg/m-s)	$1.48\text{x}10^{-5}$	$8.76\text{x}10^{-6}$	$1.8207\text{x}10^{-5}$
γ	1.3	1.4	1.4
c_p (J/kg-K)	844	14310	1005
Pr	0.8555	0.6944	0.753
d_m (Å)	4.64	2.89	4.19

Table 2.2 shows the density ρ, specific heat c_p, and thermal conductivity k of the solids used in this investigation. The solids selected, aluminum oxide and titanium, are commonly used as spacecraft materials. The three gases are selected to represent a range of planetary atmospheres: air (Earth), carbon dioxide (Mars and Venus), and hydrogen (Jupiter, Saturn, Uranus, and Neptune). The thermal accommodation coefficient σ_T assumed to be 1 for all the gases throughout in this investigation (Yamaguchi, 2012 and Zhou, 2010).

Table 2.2. Solid Properties

Property	**Aluminum Oxide (99.5%)**	**Titanium**
k_s (W/m-K)	35	21.9
ρ (kg/m^3)	3890	4506
c_p (J/kg-K)	880	523

Initial simulations use the combination of Al_2O_3 and air to study the effects of the Knudsen number with the most common boundary conditions found in practice: 1) steady-state, 2) step increase and 3) periodic sinusoidal boundary conditions. The initial conditions throughout in this investigation for the range of x from 0 to L are kept same as the boundary condition at $x = 0$, which is temperature T_o = 280 K. The pressure and density of the gases are calculated with the ideal gas assumption and the mean free path equation (1.2) over the range of the Knudsen number 0.001 to 0.1. The temperature increment ΔT for the boundary at $x = L$ for all cases is 20 K. For the periodic boundary case, the frequency is varied between 100 Hz to as high as 10 kHz to investigate the effects until penetration depth become dominant along the length of the solid material.

2.5. Steady State

For steady-state, a constant temperature T_o is applied at $x = 0$ with an additional temperature increment of ΔT at $x = L$. The boundary conditions are as follows:

$$T(x=0)=T_o, \tag{2.16}$$

$$T(x=L)=T_o+\Delta T \tag{2.17}$$

where T_o is 280 K, ΔT is 20 K with a gas pressure and density corresponding to the Knudsen number in the entire slip flow regime i.e. from 0 to 0.1 and the slot size (L_g) of 100 microns.

The analytical solution for the steady state case is given in non-dimensional form $\theta(\xi)$ by equation (2.18) for the corresponding boundary conditions of $\theta(0)=0$, and $\theta(3)=1$. $\Delta\theta$ as function of K_{nL} at the solid-gas interfaces ξ=1 and ξ=2 is given by equation (2.19).

$$\theta(\xi)=\begin{cases}\dfrac{\frac{k_g}{k_s}\xi}{1+2\cdot\left(Kn_L C+\frac{k_g}{k_s}\right)} & for\ 0\le\xi\le 1\\[2ex] \dfrac{\xi-1+Kn_L C+\frac{k_g}{k_s}}{1+2\cdot\left(Kn_L C+\frac{k_g}{k_s}\right)} & for\ 1<\xi<2\\[2ex] \dfrac{1+2\cdot Kn_L C+(\xi-1)\frac{k_g}{k_s}}{1+2\cdot\left(Kn_L C+\frac{k_g}{k_s}\right)} & for\ 2\le\xi\le 3\end{cases} \tag{2.18}$$

$$\Delta\theta=\frac{Kn_L C}{1+2\cdot\left(Kn_L C+\frac{k_g}{k_s}\right)} \tag{2.19}$$

where k_g and k_s are the thermal conductivity of gas and solid respectively.

Figure 2.3 shows the temperature profile for three different Knudsen numbers along the length of the model. The non-dimensional position ξ from 0 to 1 and 2 to 3 corresponds to the solid region, while ξ from 1 to 2 corresponds to the gas region. The solid has a very small temperature

gradient due to high thermal conductivity of the solid compared to the gas. $\xi = 1$ and $\xi = 2$ corresponds to the solid-gas interfaces where a temperature jump is visible in the Figure 2.3.

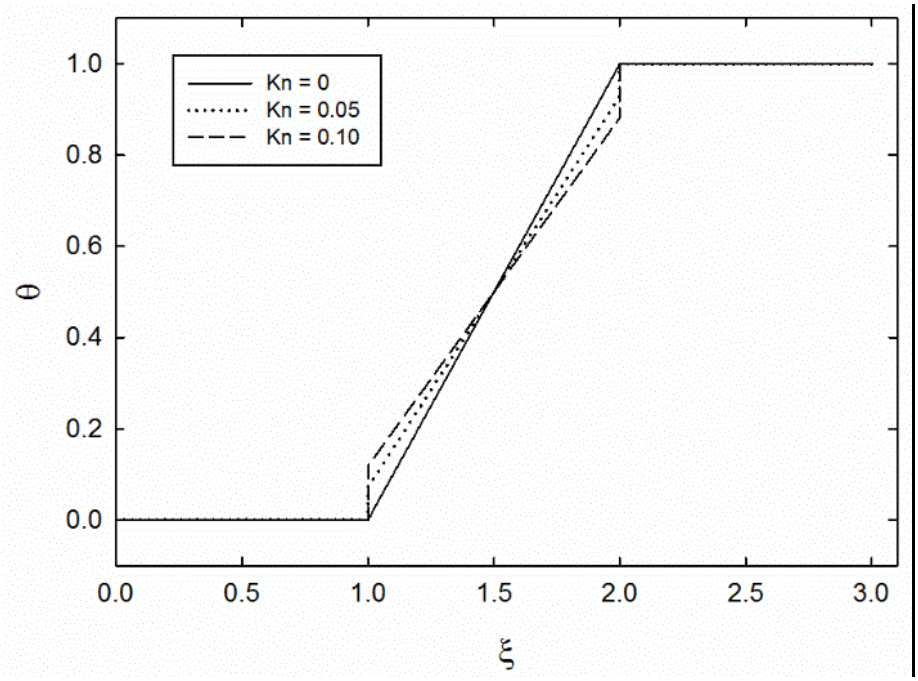

Figure 2.3. Temperature profile at different Kn for 100 microns slot size

As shown by the temperature jump equation (2.8), the temperature jump is function of the Knudsen number. Figure 2.4 shows the effects of Knudsen number on temperature profile for 100 microns slot size, which is close to average dimension of the pores. As shown in the figure, temperature jump is very small near lower boundary of the slip flow regime and increases significantly as the Knudsen number is increased. This analysis suggests possible interaction of the Knudsen number in other thermal parameters also which needs to be investigated.

The heat flux is also investigated for the effects of the Knudsen numbers. Figure 2.5 shows normalized heat flux vs Knudsen number plot for slip flow regime. Heat flux (q'') at respective Knudsen numbers is normalized by the heat flux (q_c'') in continuum flow i.e. Kn < 10^{-3} (Zhou, 2010). As shown in the figure, normalized heat flux is close to 1 at low Knudsen number in the

vicinity of continuum regime. However it drops rapidly as we move towards higher Knudsen number.

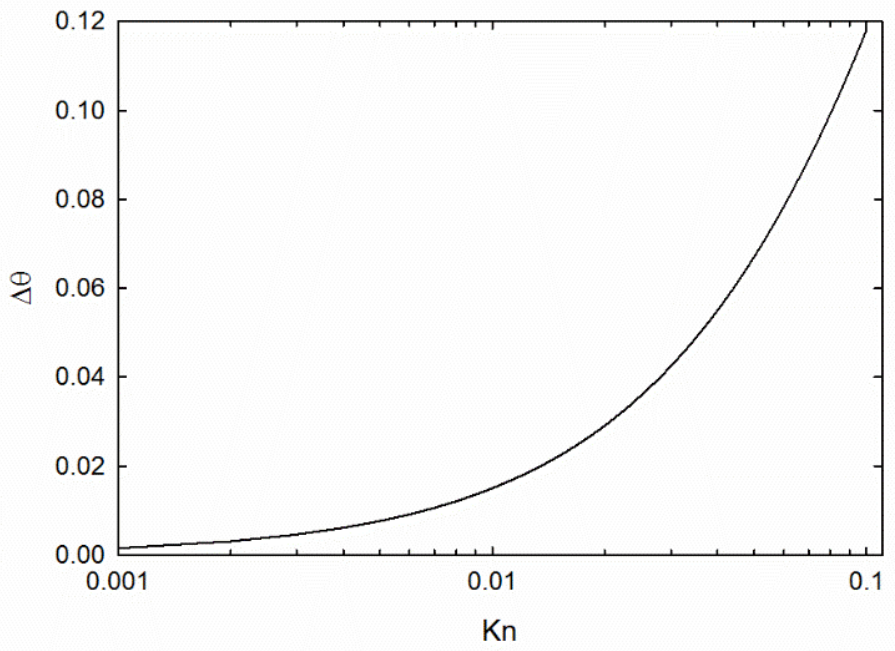

Figure 2.4. Temperature jump vs Kn for 100 microns slot size

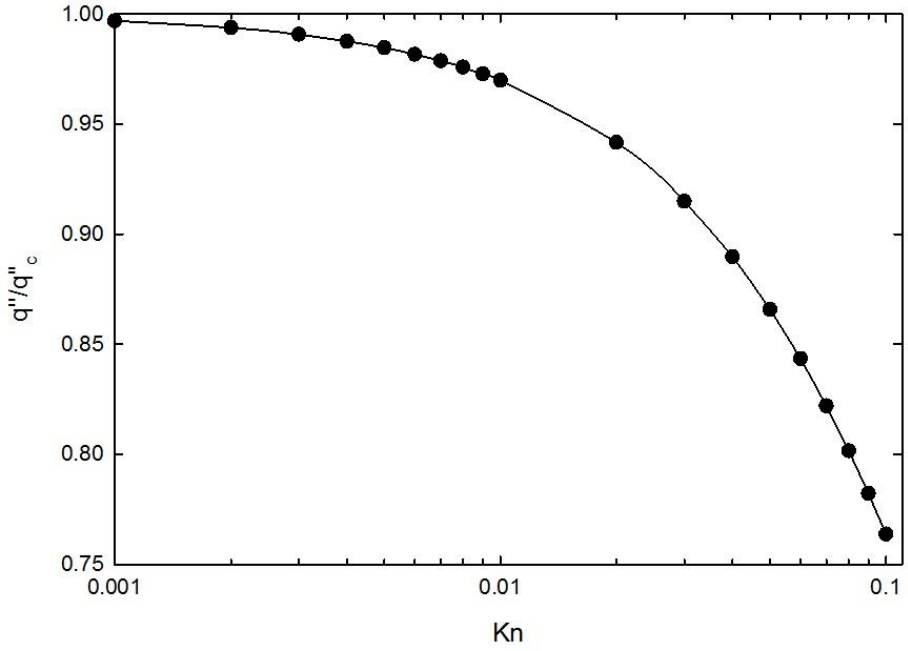

Figure 2.5. Normalized heat flux vs Kn for 100 microns slot size

2.6. Step Heating

The next case considered is the transient response to a step boundary condition. The transient analysis is carried out for a step boundary condition with initial temperature of 280 K, then abruptly changing boundary temperature at x = L to 300 K.

$$T(x=0,t)=T_o\,, \tag{2.20}$$

$$T(x=L,t>0)=T_o+\Delta T \tag{2.21}$$

where T is the temperature, L is the length defined as total length of solid and gas $(2L_s + L_g)$, ω is the angular frequency and t is the time.

Figure 2.6 shows the transient temperature profile for initial temperature 280K, boundary conditions 280K and 300K. The pressure and density of the gas corresponds to the Knudsen number of 0.01, which has been chosen at an intermediate Knudsen number such that the transient development of temperature jump at the sold-gas interfaces ξ = 1 and 2 is visible.

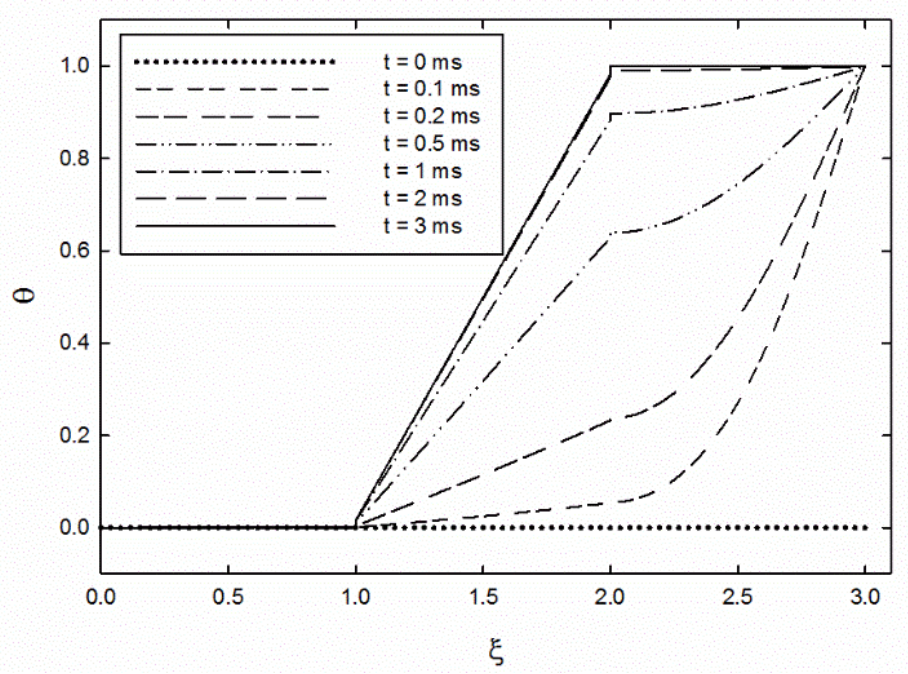

Figure 2.6. Transient temperature profile for Kn_L = 0.01 and 100 microns slot size

As shown in the Figure 2.6, as time progresses the temperature profile starts developing from the side of higher temperature boundary, and finally becomes linear as it approaches steady state. Since the temperature jump is proportional to the temperature gradient term, the magnitude of temperature jump increases as the solution approaches towards steady state.

Figure 2.7 shows the transient development of normalized heat flux profile. As shown in the figure, the heat flux in the solid is very high in the beginning because of higher temperature difference. As the solution approaching steady state, the heat flux in both solid and gas become equal which satisfies condition for steady state solution.

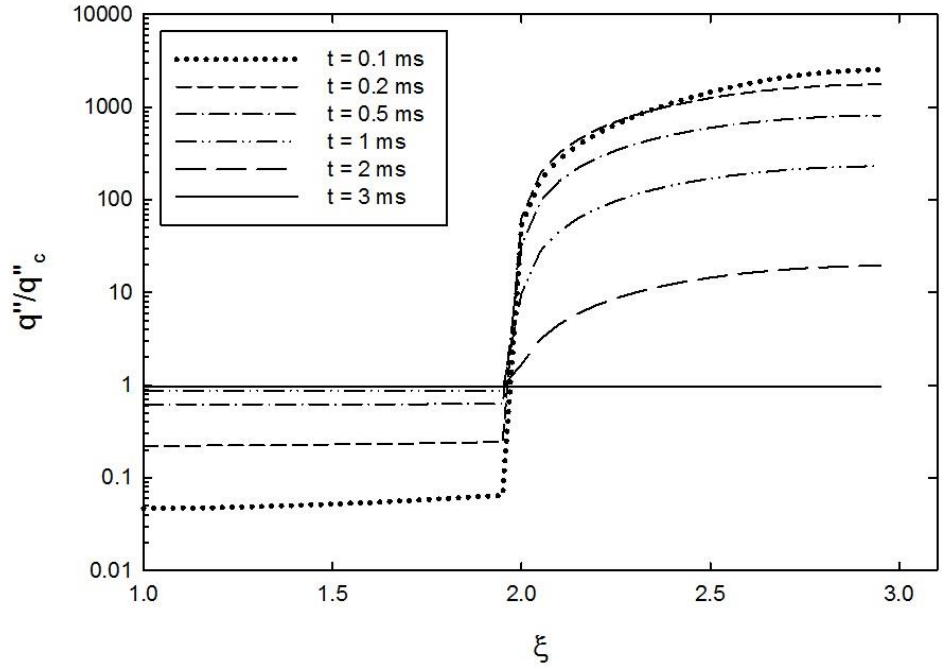

Figure 2.7. Transient heat flux profile for L = 100 μm and Kn_L = 0.01

Figure 2.8 shows the temperature jump profiles with time for different Knudsen numbers. As time progresses, the transient solution approaches the steady state solution, but the convergence rate depends on the Knudsen number. At low Knudsen numbers, the system reaches steady state more rapidly, due to the reduced interfacial resistance. This effect is partially attenuated by the increased thermal mass at lower Knudsen numbers.

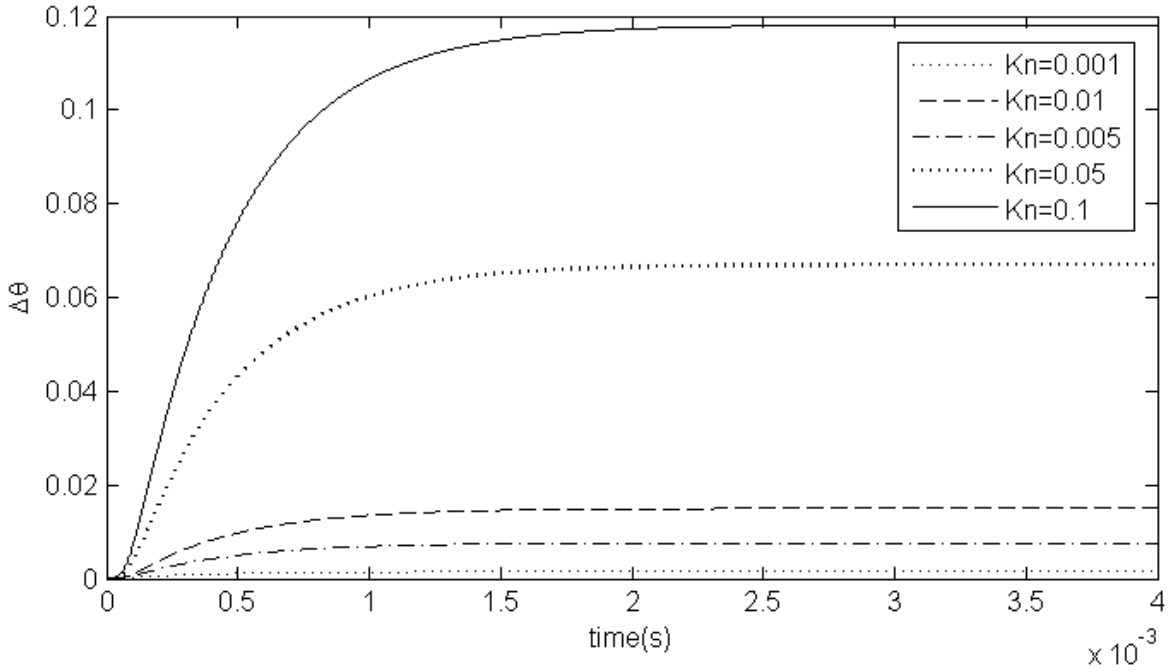

Figure 2.8. Temperature Jump vs time for different Knudsen numbers

2.7. Periodic Heating

The final case considered is a periodic sinusoidal boundary condition. For periodic boundary case, an alternate sinusoidal boundary condition is used to simulate quasi steady state temperature changes at $\xi = 3$. The boundary conditions are:

$$T(x=0,t)=T_o, \tag{2.20}$$

$$T(x=L,t)=T_o+\Delta T[1+\cos(\omega\cdot t)] \tag{2.22}$$

where ω is the angular frequency and t is the time.

The initial condition for this case is the temperature of 280 K. The pressure and density of the air depend upon the target Knudsen number for each simulation. The boundary condition at $\xi = 0$ is temperature of 280 K, and at $\xi = 3$ is temperature as a cosine function of time and frequency with a mean temperature 290 K and amplitude of 10 K.

Figure 2.9 shows the temperature profile for the frequency of 1000 Hz and a Knudsen number 0.05 over half cycle at quasi-steady-state. From the figure, the temperature fluctuation are visible and travelling across the solid; penetrating further into the gas but damping out before reaching the other end.

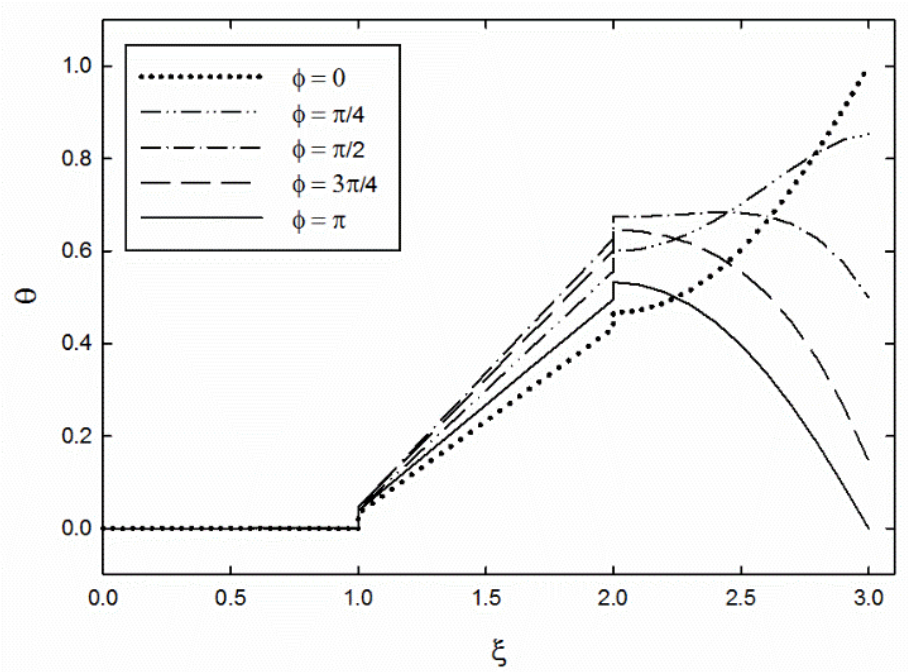

Figure 2.9. Temperature profile over half of cycle for f=1000 Hz, Kn = 0.05

The simulation frequency is increased to 10 kHz in Figure 2.10, changing the penetration depth. This gives a penetration depth that does no reach the solid-gas interface at ξ=2. The penetration depth is defined as the location from the boundary where temperature drops by 90% of the amplitude of boundary temperature. For this case penetration depth is 45 microns from the boundary at ξ=3 i.e. at location ξ=2.55. The temperature fluctuations appears to be damped out before reaching the solid-gas interface at ξ=2, hence very small change in temperature. However, fluctuations in heat flux do not disappear. Their amplitude becomes significantly small but does not die out even when it crosses solid-gas interface. This points to two variables requiring additional investigation: the amplitude and phase difference of the heat flux.

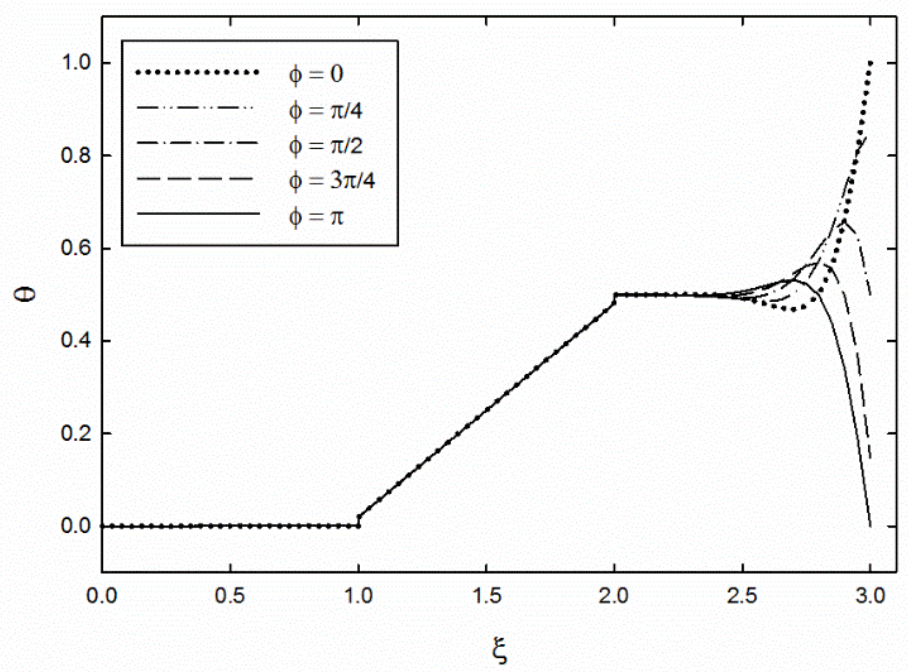

Figure 2.10. Temperature profile over half cycle for f =10 kHz, Kn = 0.025

Figure 2.11 shows the one-dimensional slot model with points marked 1-6 represent, points of interest for this investigation. Point 1 and 6 represents boundaries and points 2,3 and 4,5 represents points at solid-gas interface respectively at ξ=1 and ξ=2. Points 2 and 3 represent data of the solid at the interface and points 4 and 5 at gas.

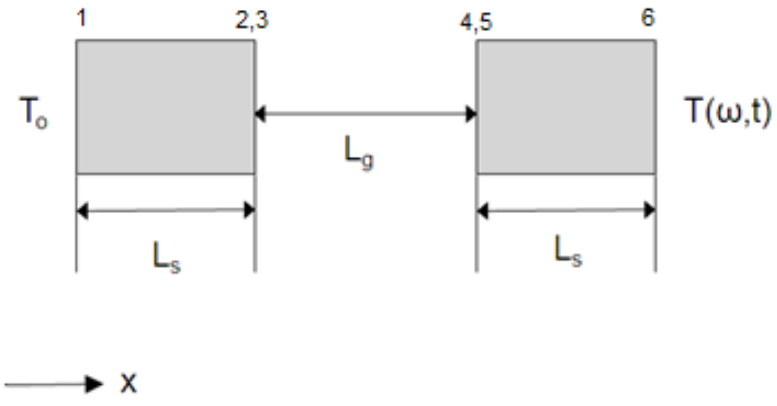

Figure 2.11. One dimensional slot model of porous media.

The transient temperature profile at points 2 through 6 marked is shown in the Figure 2.12. Since the boundary temperatures are predefined, the points belonging at the solid-gas interfaces remains of most interest for this investigation. As shown in this figure, the amplitude of temperature fluctuations is significantly higher at 4 and 5 because of proximity of periodic boundary. This focuses our interest around ξ=2. T_4 and T_5 show transient development of temperature profile at interface and appear to be out of phase from boundary conditions. Therefore the phase difference must be also investigated for any possible effects of the Knudsen number.

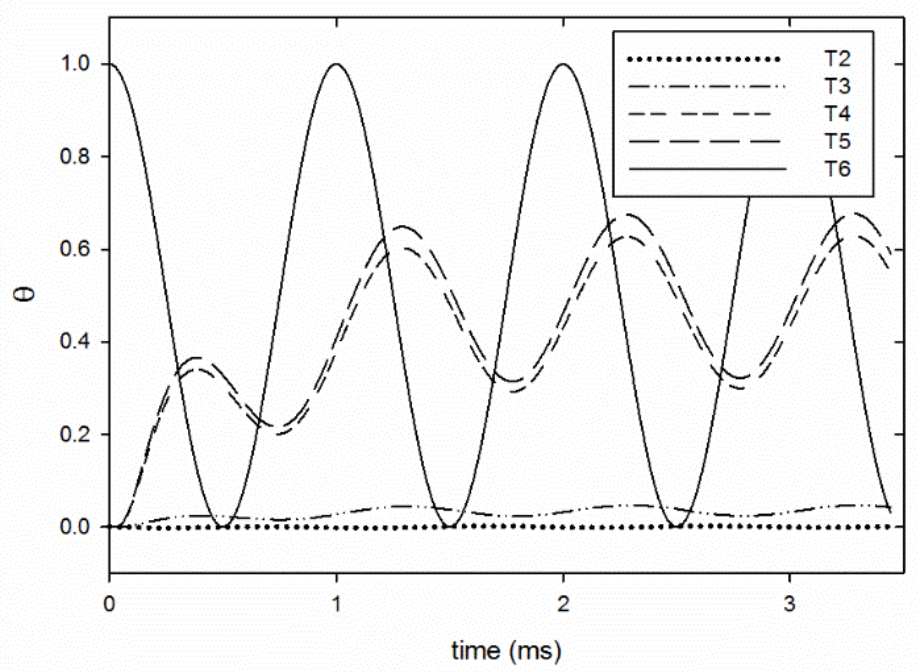

Figure 2.12. Transient temperature profile for Kn_L = 0.01 and 100 microns slot size

Additional simulations provide detailed analysis of the heat flux amplitude, phase difference and the effects of the Knudsen number, slot size and frequency. At the solid-gas interface ξ=2, both points 4 and 5 have significantly different thermal conductivity. Therefore, the difference in temperature gradient as shown in the previous steady state analysis of Figure 2.3. However, the heat flux is same at the solid-gas interface for steady state analysis. This condition will also hold true for quasi-steady state periodic boundary condition. Figure 2.13 shows that the mean heat flux

is constant and independent of the frequency. However, the amplitude of heat flux may vary between the solid and gas phases.

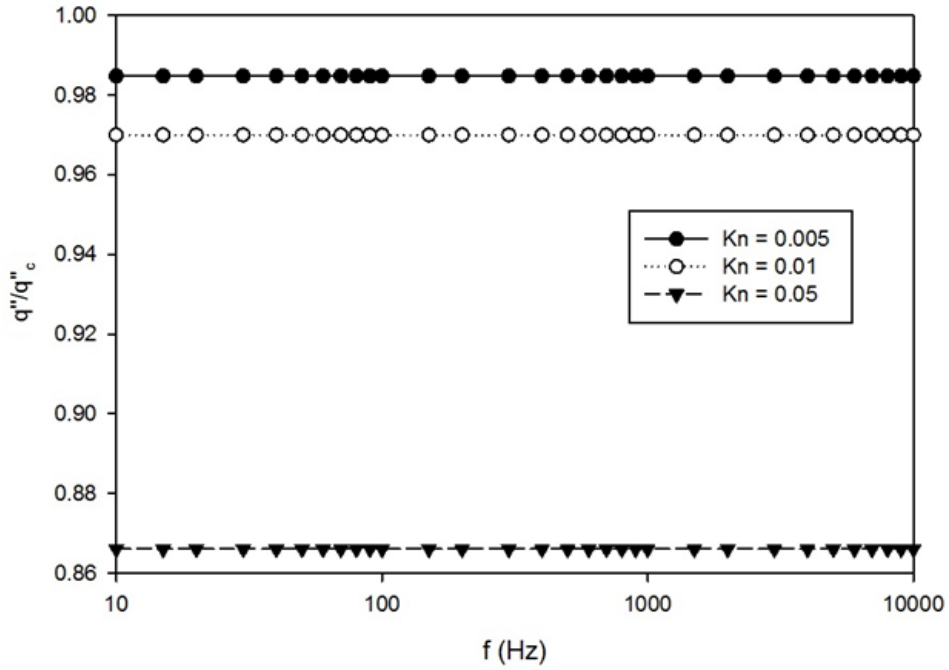

Figure 2.13. Mean heat flux in state across the one-dimensional porous model

Figure 2.14 presents the results of several simulations over the range of frequency between 100 Hz to 10 kHz, and the Knudsen number ranging between 0.001 and 0.1. Figure 2.14 shows the normalized amplitude of heat flux (q''/q_c'') in the gas at the interface at point 4. As shown earlier in the results, increasing the frequency decreases the penetration depth hence. Therefore, the amplitude of the fluctuation, are likely to decrease. Figure 2.14 gives a similar picture frequency versus amplitude relationship. As shown in the figure amplitude decreases as frequency of periodic heating increases and finally approaching towards zero as penetration depth become significantly small to allow any fluctuations to reach at the interface. As the frequency changes, the Knudsen number also affects the amplitude. The heat flux amplitude decreases as Knudsen number increases. However the effects are greater at larger Knudsen numbers.

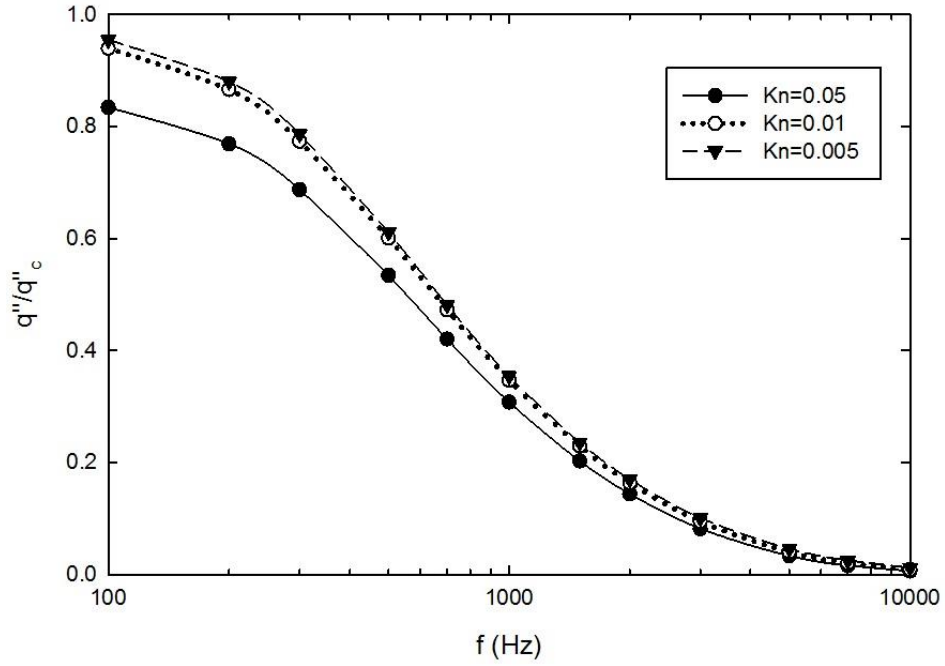

Figure 2.14. Amplitude of heat flux in the gas at the interface (point 4, Figure 2.11)

Figure 2.15 presents the heat flux amplitude for solid region at the solid-gas interface, represented as point 5. However, the results show completely different behavior than previously speculated relationship between the amplitude and frequency based on the penetration depth. Unlike point 4 i.e. gas region at the interface where amplitudes decreases with increase in frequency, point 5 approaches a maxima around 1000 Hz. This indicates towards a possible resonance which increases the fluctuations. However, as the frequency increases, the heat flux amplitude also decreases due to decrease in the penetration depth. The effects of Knudsen number on the heat flux amplitude at the two different edges of the gas phase are the same. The effects of the Knudsen number on the heat flux amplitude in the solid region of the interface increases as the Knudsen number increases.

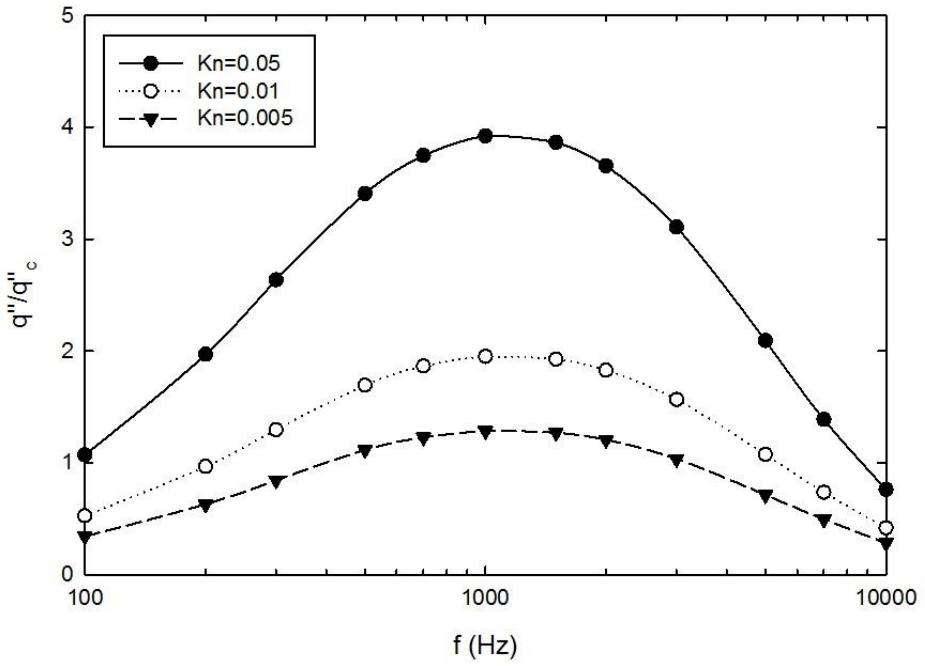

Figure 2.15. Amplitude of heat flux in the solid at the interface (point 5, Figure 2.11)

Previous results showed that the temperature profile at the interface is out of phase relative the periodic boundary condition. Therefore, the heat flux amplitude may also have a phase difference ϕ. As shown previously, despite the equal mean heat flux across the interface, the instantaneous amplitude varies with frequencies. Therefore the normalized heat flux profile of point 4 and 5 is compared for the analysis of the phase difference. Figure 2.16 shows the heat flux profile of both solid and gas region over a cycle in quasi-steady-state across the interface is plotted against each other. The plot shows that the apart from the difference in the heat flux amplitude, there is a phase difference between the heat fluxes across the solid-gas interface. This phase difference may vary with frequencies and the Knudsen number also. Therefore, the phase difference will be investigated for a possible relationship against the frequencies and the Knudsen numbers.

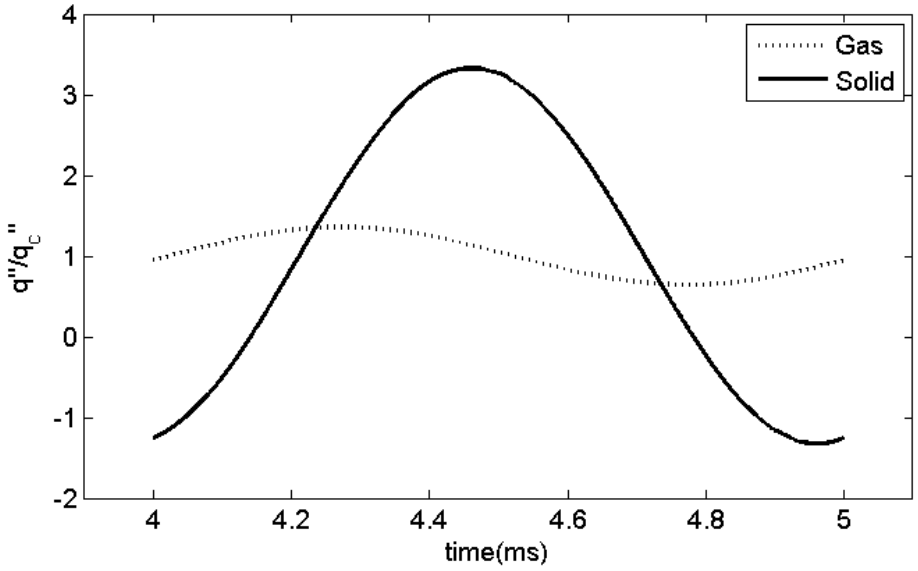

Figure 2.16. Normalized heat flux at the interface (point 4 and 5, Figure 2.12)

Figure 2.17 presents the phase difference between heat flux at point 4 and 5 relative to the heat flux at point 6 i.e. periodic boundary. The results shows that the phase difference at both points 4 and 5 increases monotonically with an increase in frequency. However, the relative phase difference between the phase of point 4 and 5 decreases as the frequency increases.

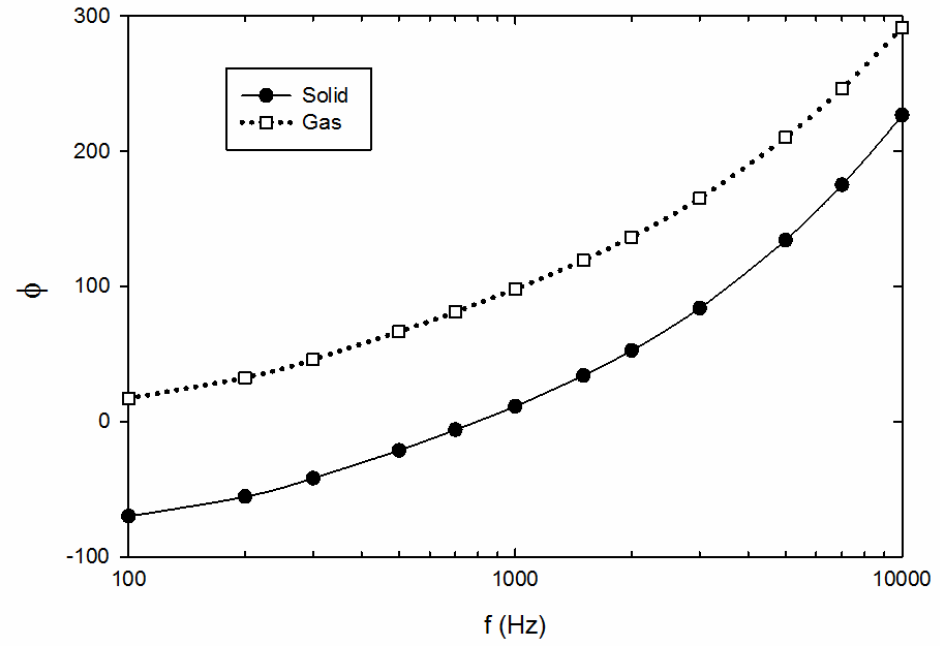

Figure 2.17. Phase difference between heat fluxes at the interface and boundary

The phase difference in heat flux across the interface at point 4 and 5 is also examined. As shown in the Figure 2.18 phase difference appears to be decreasing with an increase in frequency which depict similar behavior speculated earlier because of decrease in penetration depth with an increase in frequency. The Knudsen number has a significant effect on phase difference. However unlike the heat flux amplitude, the phase difference increases with an increase in Kn and phase difference become significantly larger for higher frequencies.

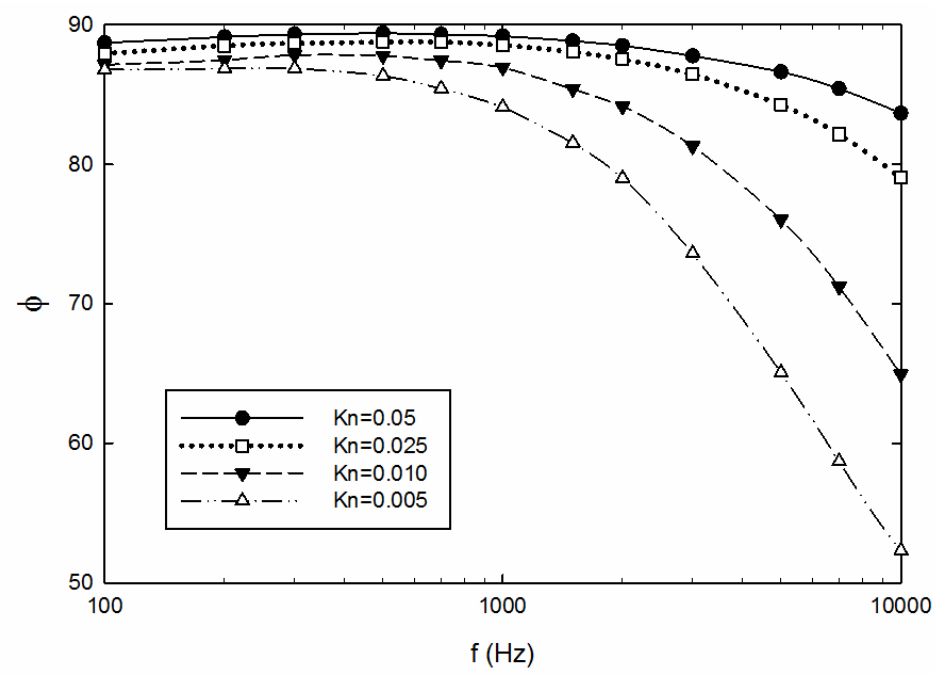

Figure 2.18. Phase difference between heat fluxes across the interface (point 4, 5)

After studying the effects of Knudsen number, the effects of slot sizes relative to solid size are also investigated. When the slot size is changed, it changes the characteristic length, which is closely associated with the mean free path and the Knudsen number thus affecting the results. Figure 2.19 presents the phase difference across the interface; point 4 and 5 for various simulations over the range of frequency and a fixed $Kn = 0.01$ with different slot sizes 50 microns, 100 microns and 200 microns. As shown in the figure, phase difference decreases as we move towards higher frequencies. However, for lower frequencies, the phase difference encounters a point of inflection

around 300 Hz. The phase difference seems to increase with decrease in the slot size which might be because of the facts that decreasing the slot size is against moving closer towards mean free path, hence kinetic effects of the gases become dominant.

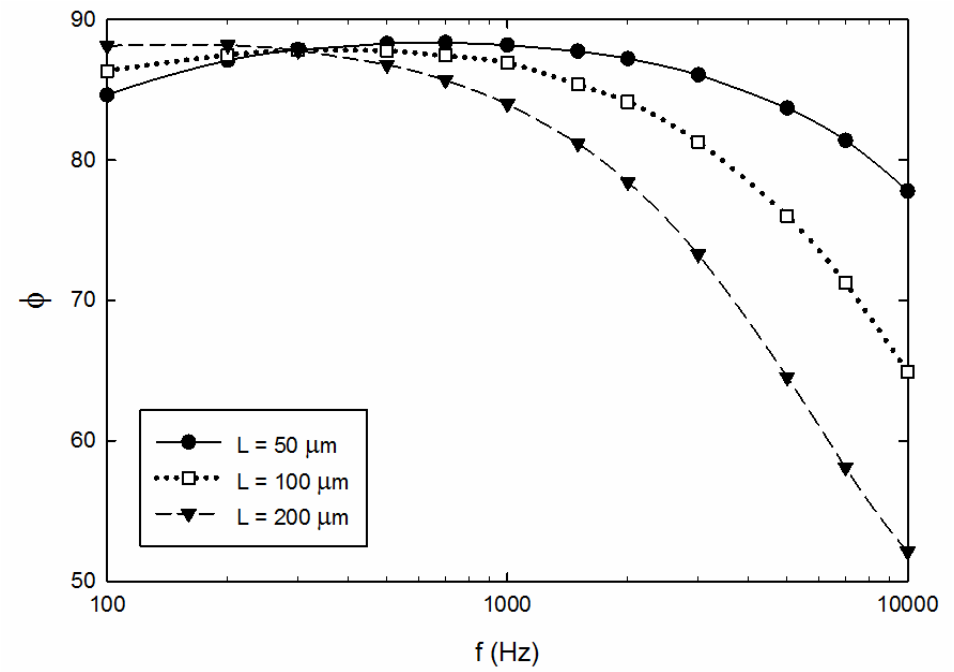

Figure 2.19. Phase difference between heat fluxes across the interface (point 4, 5)

Figure 2.20 shows the effects of the Knudsen numbers on phase difference for a constant frequency. As shown in the figure, phase difference is unaffected for the continuum region. But as the Knudsen number crosses continuum region and enters in slip flow, it affected significantly because the temperature jump condition becomes significant. When the Knudsen number is increased further, the rate of increment in the phase difference decreases, which demonstrate that the temperature jump condition is significant only in the slip flow region. If the Knudsen number increases into the transition region, the temperature jump equation will not be valid anymore, requiring simulation techniques based on kinetic theory.

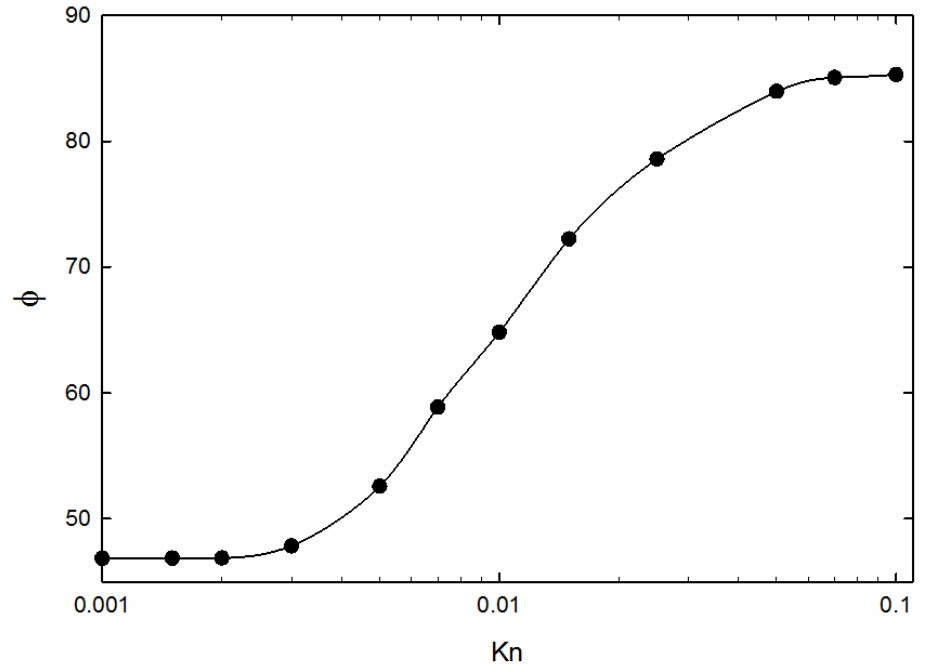

Figure 2.20. Phase difference vs Kn for f = 10 kHz and 100 microns slot size

2.8. Effects of Gases

Previous investigation considered only Al_2O_3 and air as the solid-gas combination. However, when insulations are used in the different environments, the effects of gas properties must be considered to capture the general thermal behavior of porous media. Three gases: air (79% N_2 and 21% O_2 by volume), hydrogen (H_2) and carbon dioxide (CO_2) has been compared to study the effects on similar parameter as previous cases using Al_2O_3 as common solid material.

Similar to previous investigation, the steady-state heat transfer is simulated for all three gases. Figure 2.21 compares the steady state temperature profile. As shown in the figure, the non-dimensional temperature profile changes inside the slot, where the effects are most noticeable. The temperature gradient inside the slot is different for each gas because of the difference in thermal conductivity.

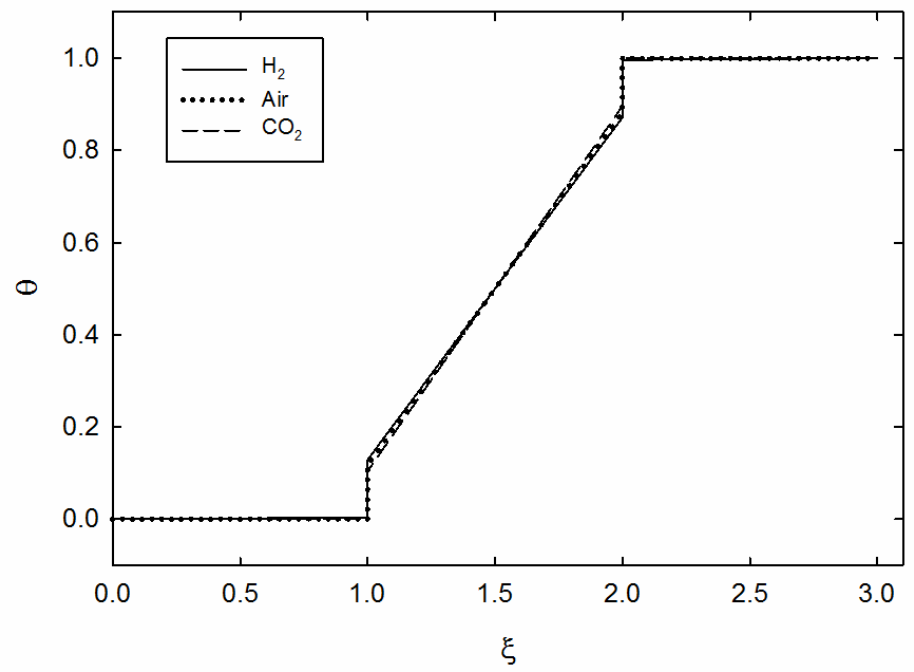

Figure 2.21. Steady state temperature profile of gases at Kn = 0.1

Figure 2.22 shows the temperature jump for the three gases over the range of the Knudsen number. The temperature jump is almost negligible for all three gases for lower range of the Knudsen number. However as the Knudsen number increases, both the temperature jump, and the difference between the gases increases. This appears to be driven by the change in Prandtl number between the gases, which appears in the temperature jump equation. The temperature jump is inversely proportional to the Prandtl number. Hence, the temperature jump is higher for the gas with lower Prandtl number.

The normalized heat flux (q''/q_c'') is also investigated for the gases. Figure 2.23 shows that the apart from the effects of Kn, gas properties also affect heat fluxes. As shown in the figure, for a fixed Kn, all the gases have different value of (q''/q_c''), and it appears to be following the same order of their respective Prandtl numbers.

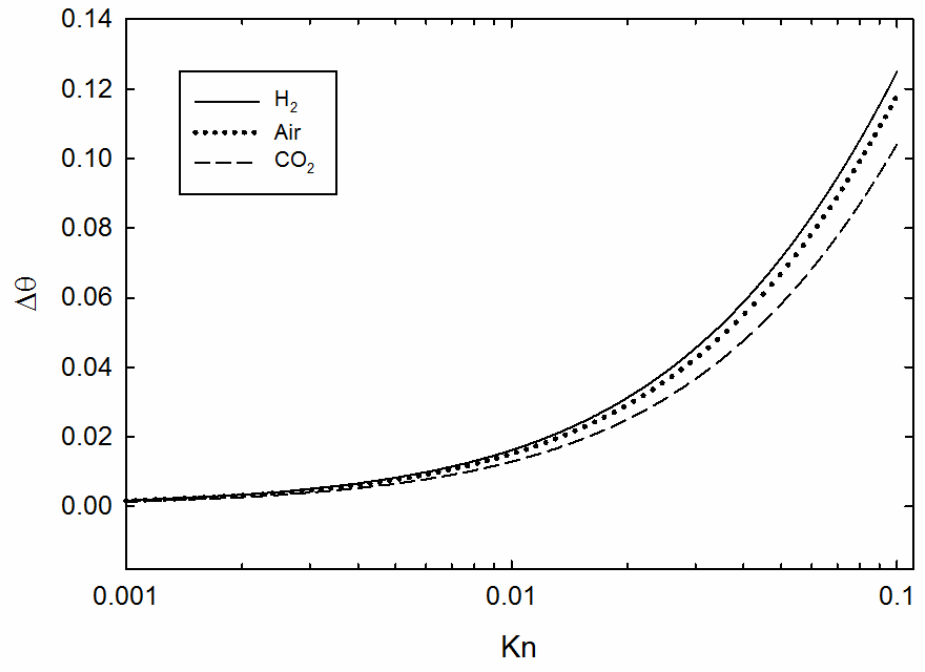

Figure 2.22. Temperature jump over the range of Kn in slip flow regime

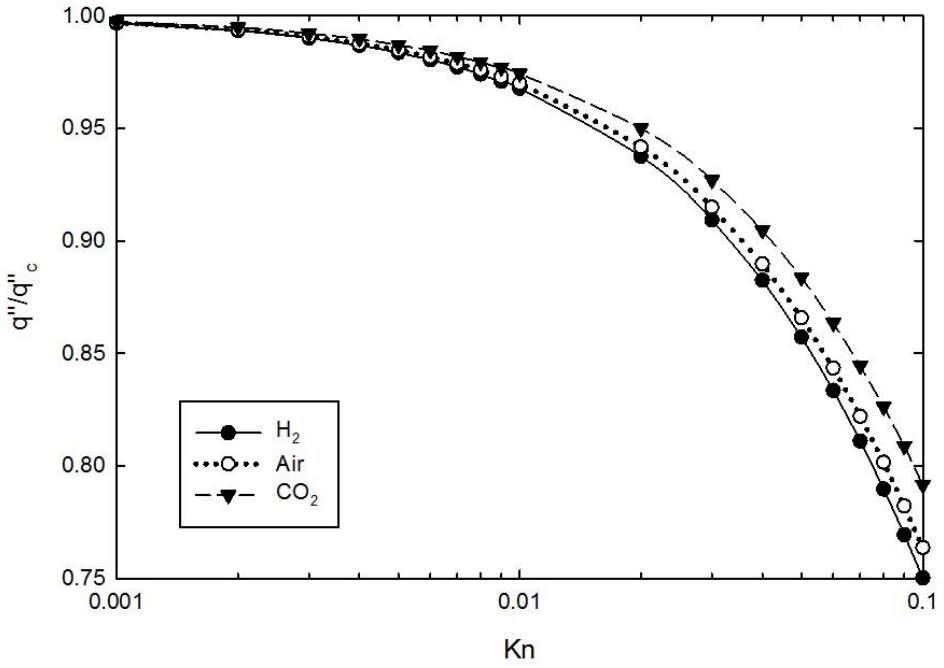

Figure 2.23. Normalized heat flux vs Kn in slip flow regime

The transient response to a step boundary condition is simulated. Figure 2.24 shows the temperature jump evolving with the time for all three gases. As with the steady case, the gas with the lowest Prandtl number has the largest temperature jump.

The study of periodic boundary heating is repeated with all three gases. However, unlike the previous case instead of Knudsen number, gases are compared for their impact on the parameters for a given Knudsen number over the range of the frequency. Because the effect of changing gases appeared to be largest at low frequency, the range of frequencies shown is extended down to 10 Hz.

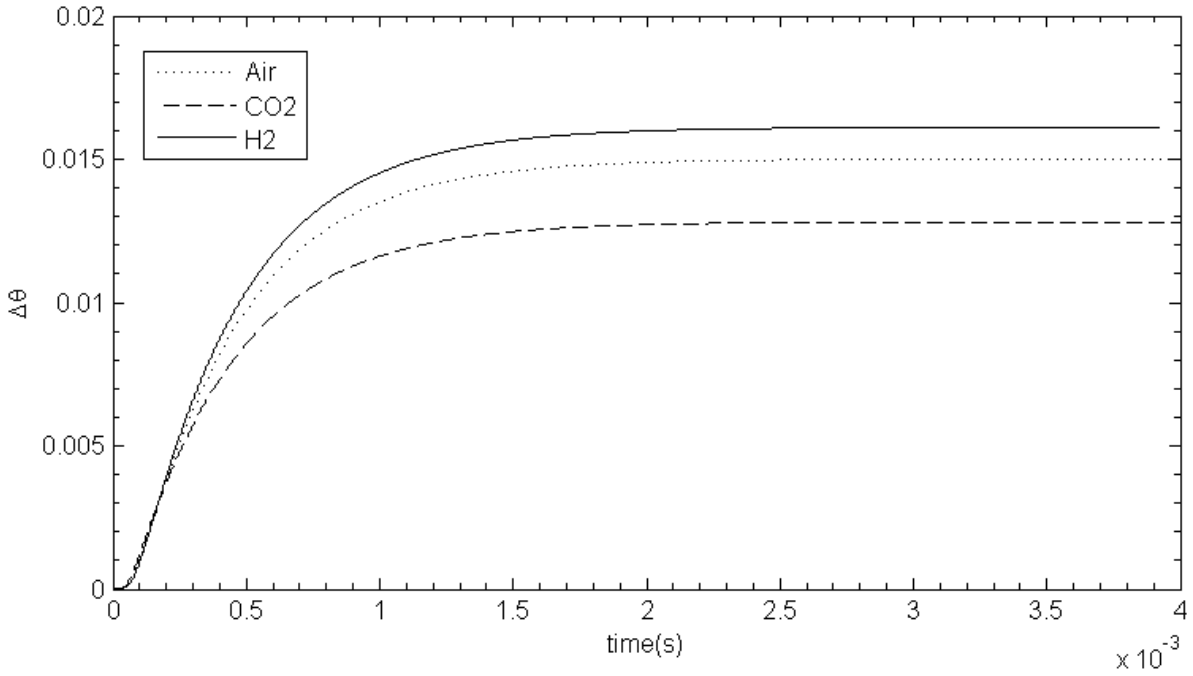

Figure 2.24. Temperature jump in transient case for gases at Kn = 0.01

Figure 2.25 shows the impact of the gases on normalized heat flux amplitude (q''/q_c'') for a given Kn = 0.01 over the range of frequency. The results shows the normalized amplitude of heat flux on the gas side of the solid-gas interface is not affected by the choice of the gas. However, at the solid side of the interface, it is not the case. Figure 2.26 shows that the gas has a direct impact of the normalized heat flux amplitude on the solid side of the interface due to the Prandtl number.

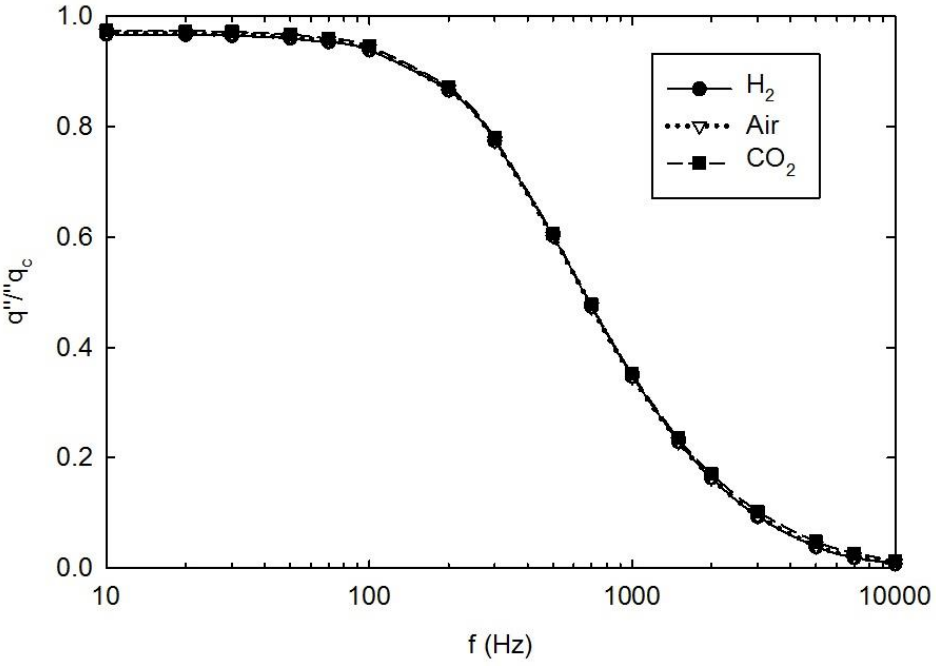

Figure 2.25. Amplitude of heat flux at the interface in gas at Kn = 0.01

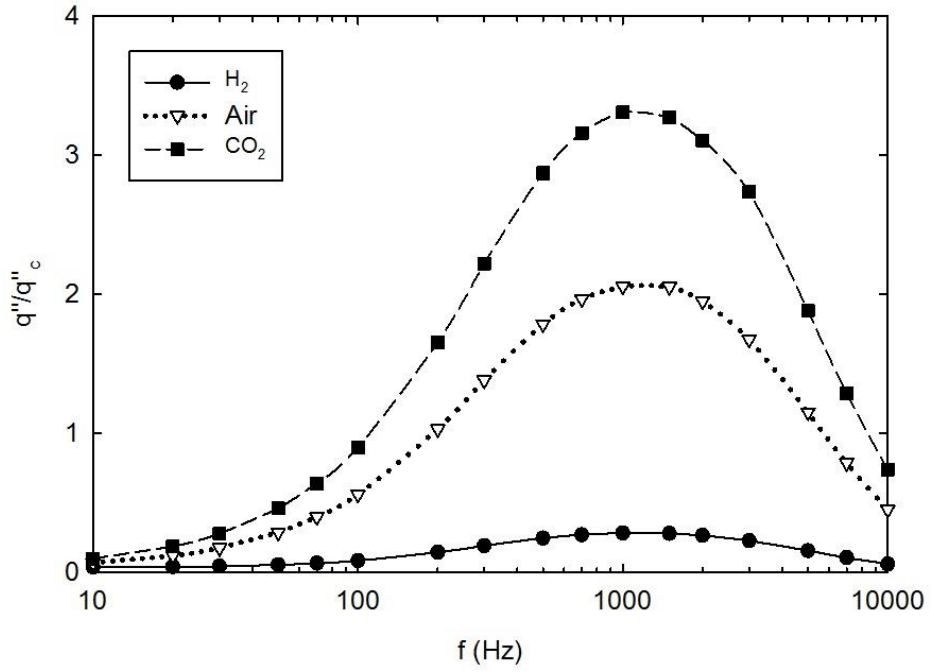

Figure 2.26. Amplitude of heat flux at the interface in solid at Kn = 0.01

Figure 2.27 shows the phase difference for Kn=0.01 over the range of frequency from 10 Hz to 10 kHz. As shown in the figure, the phase difference in heat flux at the solid-gas interface depends on the choice of the gas. The effect of Knudsen number on the phase difference varies significantly from gas to gas. As previously shown in Figure 2.18 for air, irrespective of Knudsen numbers the phase of heat flux does not significantly change at lower frequencies between 100 Hz and 1000 Hz. However, Figure 2.27 shows that the heat transfer of a hydrogen system is very sensitive to changes in Knudsen number.

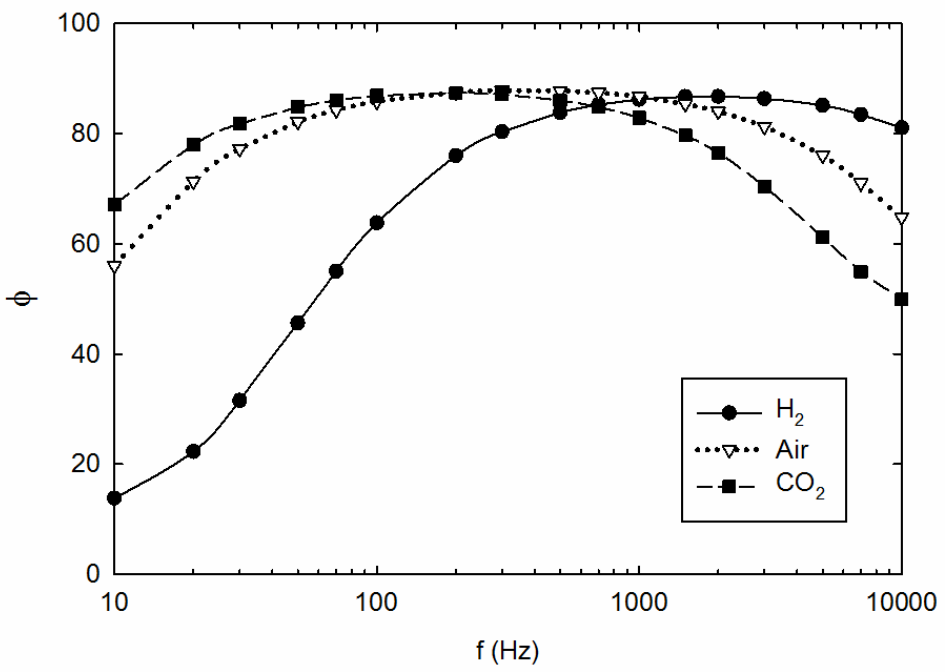

Figure 2.27. Phase difference in heat flux at the interface at Kn = 0.01

Figure 2.28 shows the behavior of 3 different gases with an excitation at 10k hz over the range of Knudsen number. As seen before, hydrogen is much more sensitive than air and carbon dioxide towards the changes in the Knudsen number. The results for hydrogen show changes due to Knudsen number effect at much lower values than air or carbon dioxide.

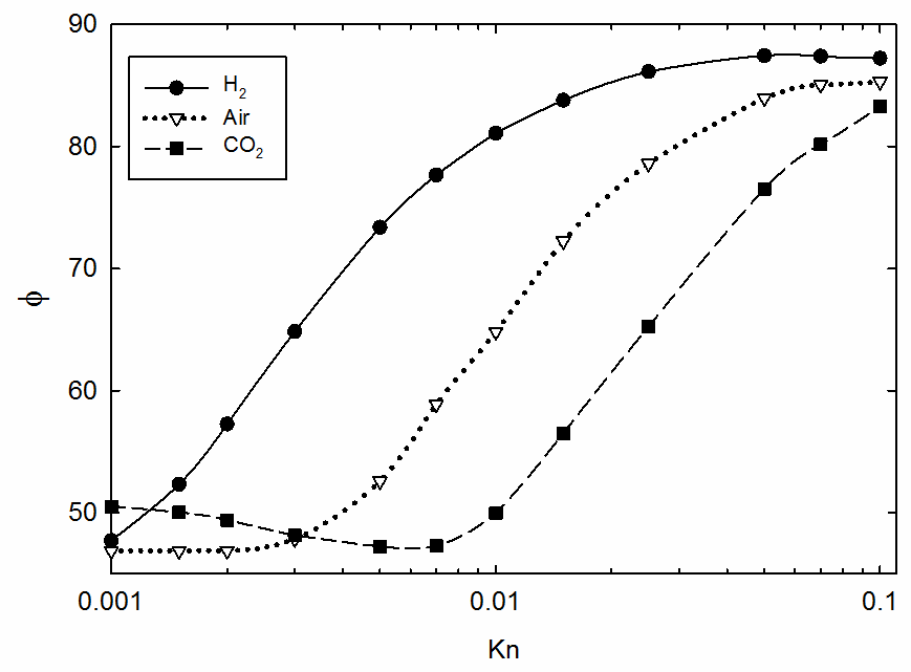

Figure 2.28. Phase difference in heat flux at the interface over a range of Kn

2.9. Effects of Solid Materials

The effects of the solid materials are also investigated. Al_2O_3 and Titanium (Ti) are compared for this part of the investigation because of the difference in their thermal properties. Figure 2.29 shows steady state solution for both materials considering air as common gas. The results shows that there is not any noticeable difference in the temperature profile because of the fact that thermal resistance of the gas is much higher hence the effects are dominated by the gas considering the slot size of 100 microns. Similarly, Figure 2.30 shows the temperature jump over the range of Knudsen number, and Figure 2.31 shows normalized heat fluxes. In all three cases, the plots almost overlap because of overall thermal resistance is dominated by the gas phase, not the solid phase. Therefore, the choice of solid material is relatively unimportant in computing the overall thermal behaviour of the system.

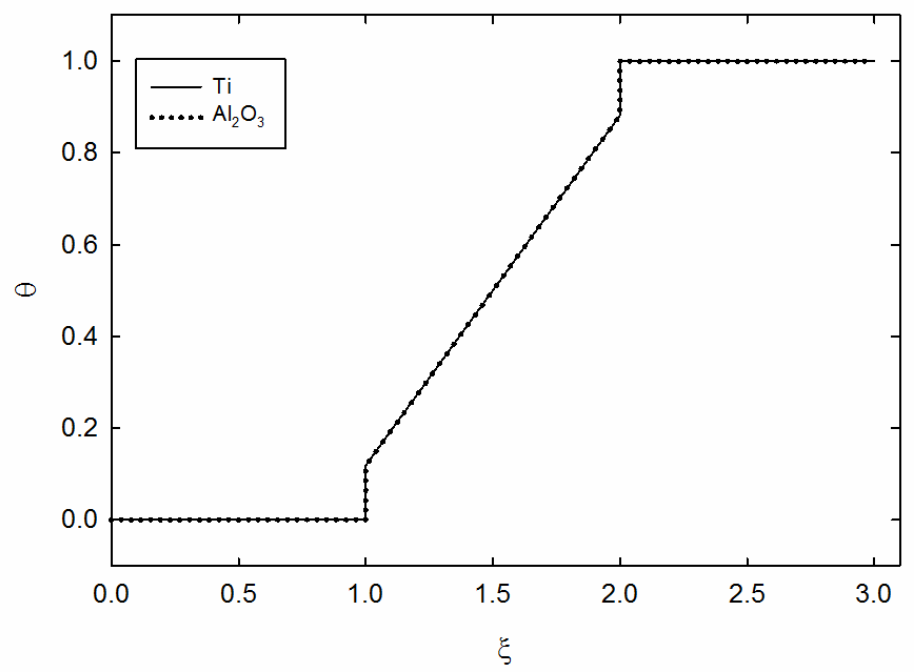

Figure 2.29. Steady state temperature profile for Kn=0.1 for solids

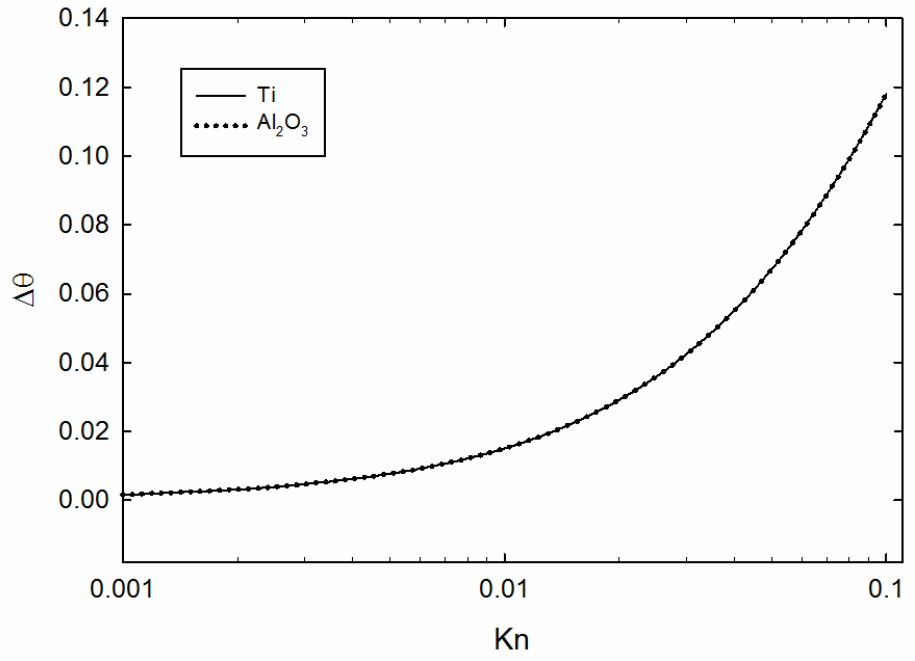

Figure 2.30. Temperature jump over the range of Kn for solids.

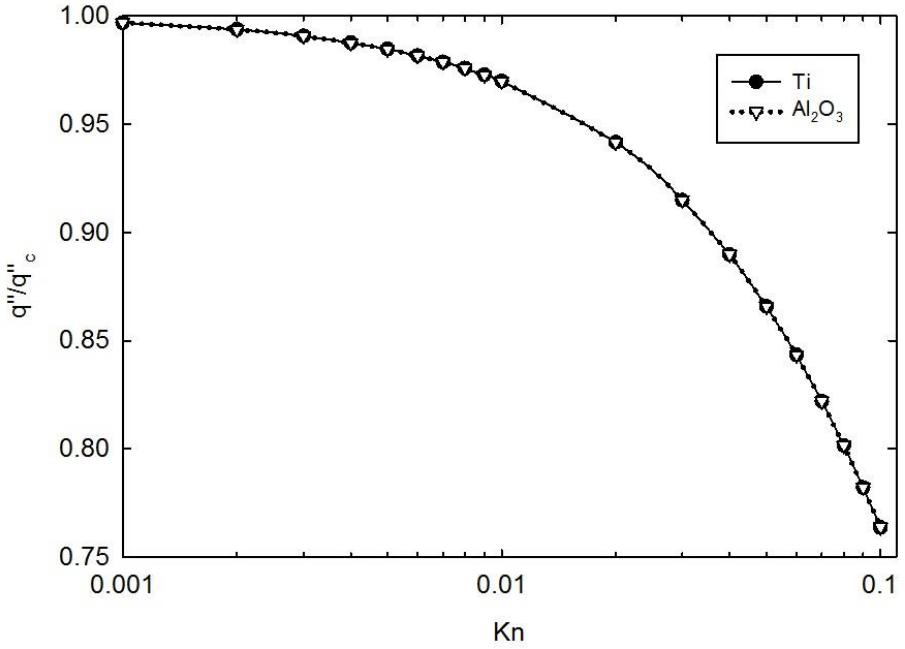

Figure 2.31. Normalized heat flux vs Kn for solids

Figure 2.32 shows the transient temperature profile for step boundary condition. The results show that the choice of the solid doesn't have any effect on temperature jump. However the rate of convergence is higher for Al_2O_3 due to higher thermal conductivity.

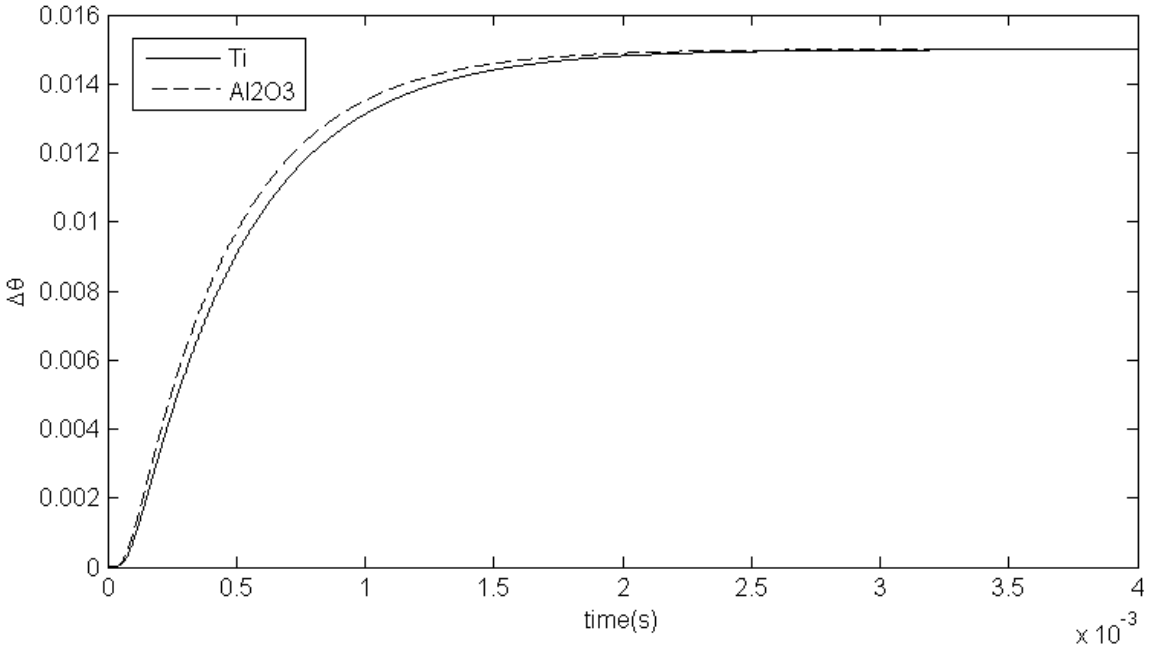

Figure 2.32. Temperature jump in transient case at Kn=0.01

Similar to previous investigation, periodic boundary conditions are also simulated to study the effects of the solids. Figure 2.33 shows the impact of the choice of the solid materials on the normalized heat flux amplitude in gas region at solid-gas interface for a given Kn = 0.01 over the range of frequency. The results show that the normalized heat flux does not changes significantly based on the choice of the solid because.

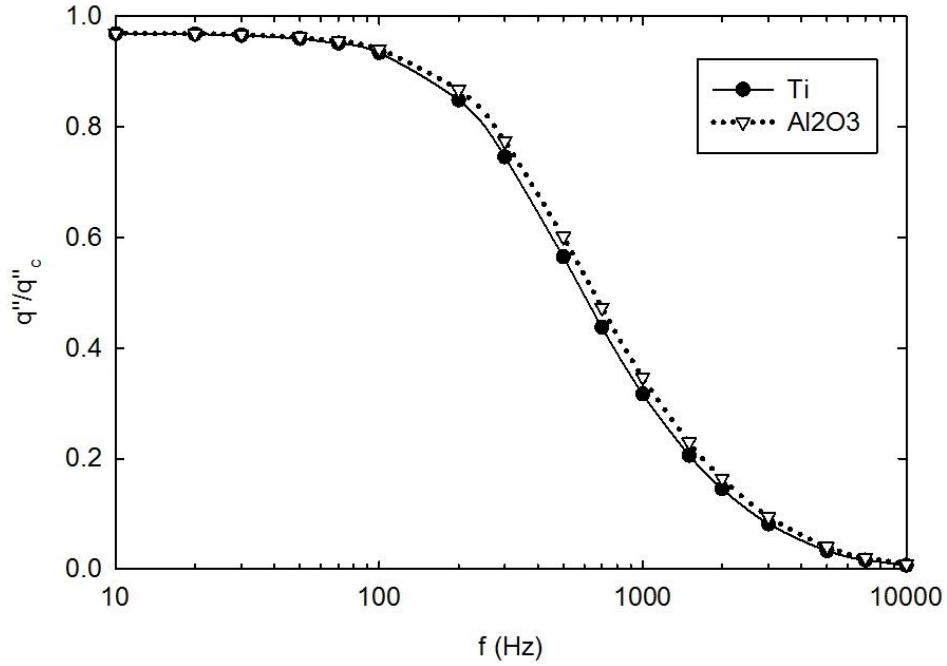

Figure 2.33. Heat flux amplitude at the interface in gas at Kn=0.01

Figure 2.34 shows the amplitude on the solid sides of the interface. Since air is used for both the cases, the Knudsen number is also fixed. The heat flux amplitude change sigificantly for both solids. The fluctuations show similar behavior of resonance as previsouly observed. The maximum amplitude of the fluctuations is at ~1000 Hz. However, as the frequency increases, penetration depth changes the, and the fluctuations reduce significantly.

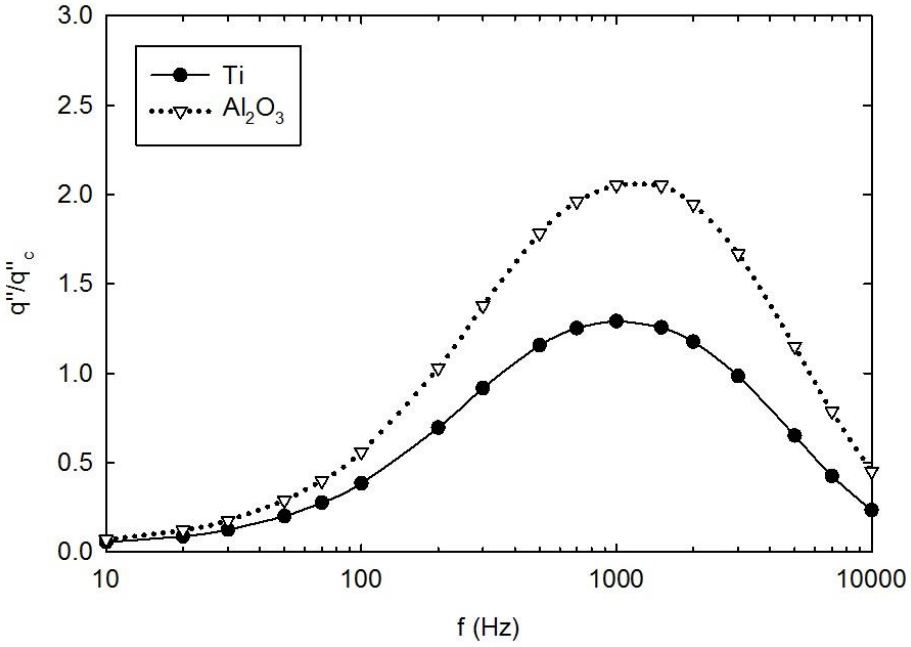

Figure 2.34. Heat flux amplitude at the interface in solids at Kn=0.01

The phase difference is also investigated. However, unlike previous results, the phase difference does not change with the choice of metal, except at lower frequencies with a fixed Knudsen number, as shown in the Figure 2.35 and Figure 2.36.

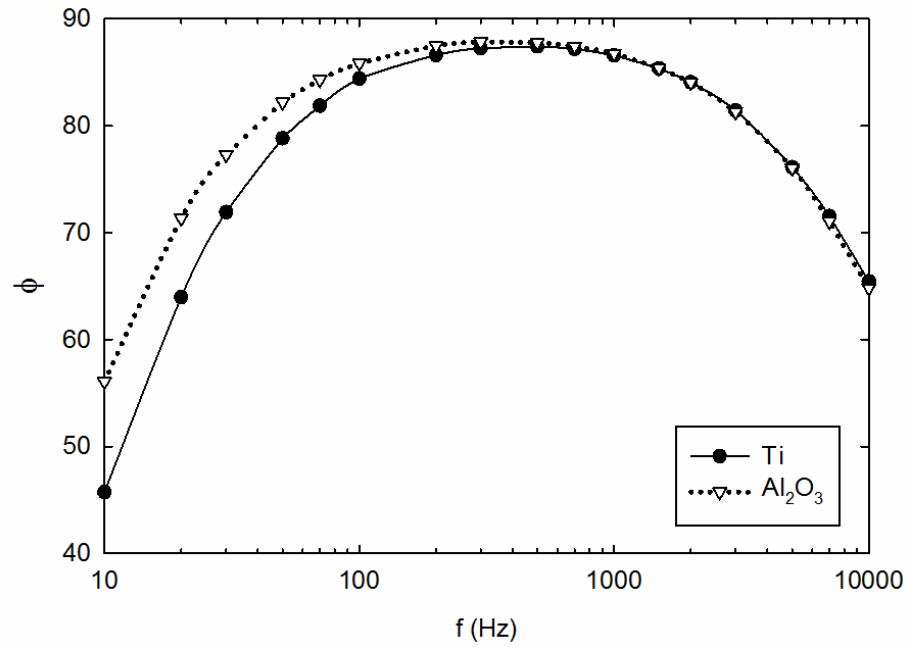

Figure 2.35 . Phase difference at the interface for solids at Kn=0.01

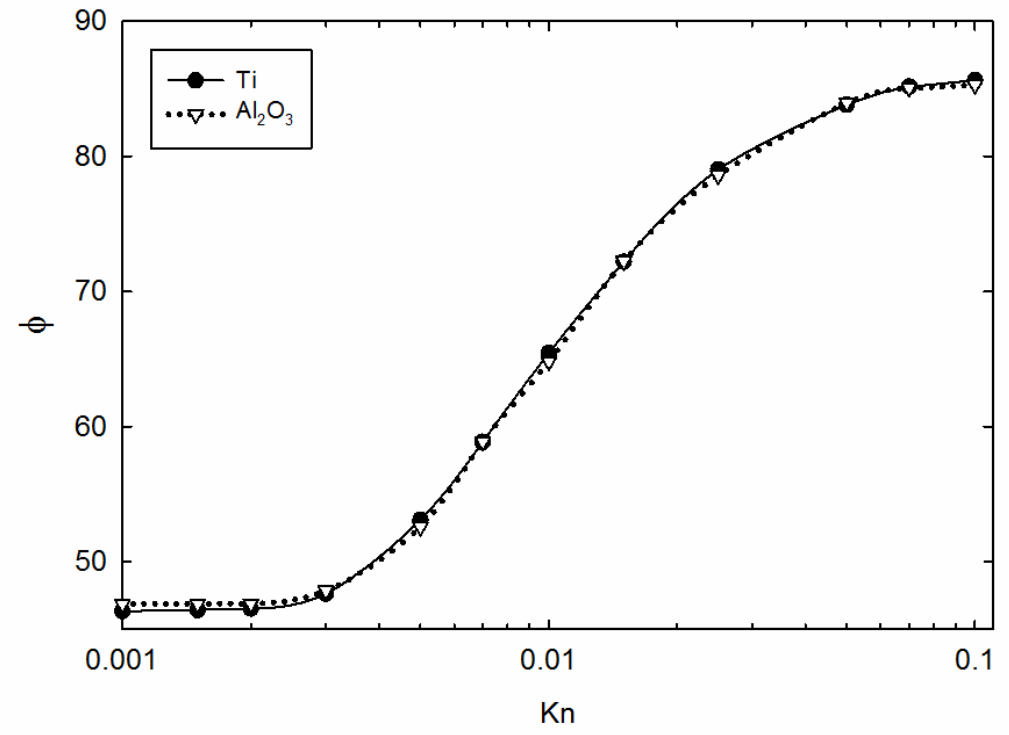

Figure 2.36. Phase difference at the interface for solids over a range of Kn

2.10. Concluding Remarks

A one-dimensional slot model of porous media has been investigated with a temperature jump equation. The model consists of solid material with a gas trapped inside the slot of the order of 100 micro meters. At this length scale with low temperature and pressure range, the gas falls into the slip flow regime hence the Knudsen number becomes primary variable for the investigation. Analysis is performed for three most common cases; steady state, step boundary and sinusoidal heating. Results for all three cases are discussed over the range of the Knudsen number, frequency and the slot size. The effects of the Knudsen number appears to consistent throughout the analysis and shows noticeable change in the temperature jump, the heat flux amplitude and the phase difference. The effects of the Knudsen number show a non-linear behavior throughout the analysis. When a different gas is used, the Prandtl number of the gas, which has a large impact on the temperature jump, appeared to dominate the problem. Because of the relatively low thermal

resistance of the solid phase compared to the gas phase, the properties of the solid are relatively unimportant. Because the thermal resistance of the gas, and the interfacial resistance, are much larger than the thermal resistance of the solid, the solid material chosen is relatively unimportant.

Chapter 3 . Steady State Heat Transfer in Two-Dimensional Porous Media

3.1. Introduction

A two-dimensional model of the porous media is investigated for steady state heat transfer. Section 3.2 presents a physical model of two-dimensional porous media simplified with a rectangular cavity surrounded by the solid. The temperature jump condition obtained from the kinetic gas theory is used at the solid-gas interface. The model is solved using the two-dimensional heat equation (3.1) in conjunction with the temperature jump equation (1.4) at the solid-gas interfaces. The remainder of this chapter will presents the findings of two dimensional steady state heat transfer followed by the discussion of the effects of the Knudsen number/pressure, gases and pressure sensitive thermal properties on the effective thermal resistance of the porous media.

3.2. Physical Model

The two dimensional porous media is simplified as a rectangular cavity surrounded by the solids. Figure 3.1 represents a two-dimensional schematic diagram of the unit cell of the porous media. The cavity occupies 90% of the total volume of a unit cell with a characteristic length of the order of 100 microns. The left and right side boundaries are at a constant temperature with a finite temperature difference. The top and bottom boundaries are subjected to the symmetry boundary conditions. The solid phase will have a thermal conductivity k_s, a density ρ_s, and a specific heat $c_{p,s}$. The gas phase will have a thermal conductivity k_g, a density ρ_g, and a specific heat $c_{p,g}$.

As per Knudsen number discussion covered in the chapter 1, as the pressure of the gas present in the cavity decreases, the temperature jump at the solid-gas interface found by kinetic gas theory becomes significant. This results in reduced heat flux, hence a decrease in the effective thermal conductivity of unit cell of the porous media.

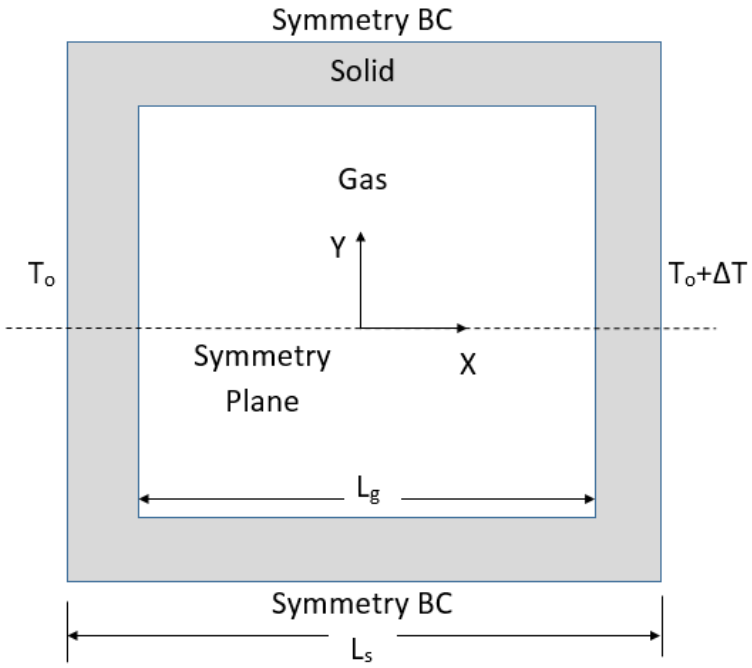

Figure 3.1. Two-dimensional schematic diagram of porous media

For the given problem, the two-dimensional heat equation (3.1) can be solved using finite difference method and explicit scheme (Jaluria, 2002). The temperature jump equation (1.4) is solved in conjunction with energy balance equation (3.2). The two-dimensional governing equations are defined as:

$$\frac{\partial^2 T}{\partial^2 x}+\frac{\partial^2 T}{\partial^2 y}=0, \tag{3.1}$$

$$k_s \left.\frac{\partial T}{\partial n}\right|_s = k_g \left.\frac{\partial T}{\partial n}\right|_g, \tag{3.2}$$

$$T_{gas}-T_w = Kn_L \cdot C \cdot \left.\frac{\partial T}{\partial n^*}\right|_{wall}, \tag{1.4}$$

$$C=\frac{2-\sigma_T}{\sigma_T}\cdot\frac{1}{\Pr}\cdot\frac{2\gamma}{\gamma+1}, \tag{1.5}$$

$$Pr=\frac{\mu c_p}{k}. \tag{2.3}$$

where *T* is the temperature, *x* and *y* are the position, *k* is thermal conductivity, the subscript '*s'* is the solid, the subscript '*g'* is the gas, *n** is the direction normal to the wall, λ is the mean free path, σ_T is the thermal accommodation coefficient, γ is the specific heat ratio, μ is the viscosity and *Pr* is the Prandtl number.

3.3. Computational Model

The equations are solved using an explicit scheme of finite difference method for the two-dimensional model of a rectangular pore with 90% cavity volume. At the solid gas interface, the temperature jump equations (1.4) is solved simultaneously with energy balance equation (3.2).

The rectangular pore is used in two-dimensional model of the porous media. The solid boundaries are also aligned with the pore. Therefore, the system can be solved in a Cartesian system using a uniform Cartesian mesh. However a finer mesh is required near the solid gas interface. This increases the overall mesh size significantly, and increasing the computation time. Therefore to reduce the mesh size and computation time, a non-uniform Cartesian mesh is used. A part of this study also focuses on multi-cell structure with higher number of cells to simulate insulation layer with finite thickness. Since the model is symmetric, only one half of the geometry is solved to further reduce the mesh size and computation time. Therefore the mesh size and the computation time play an important role, in numerical simulations. Figure 3.2 shows the non-uniform Cartesian mesh used in the model.

The non-uniform mesh is mapped to a uniform mesh, and the equations are transformed such that central difference scheme is applicable with an explicit scheme. Figure 3.3 shows the mapping of non-uniform mesh to uniform mesh.

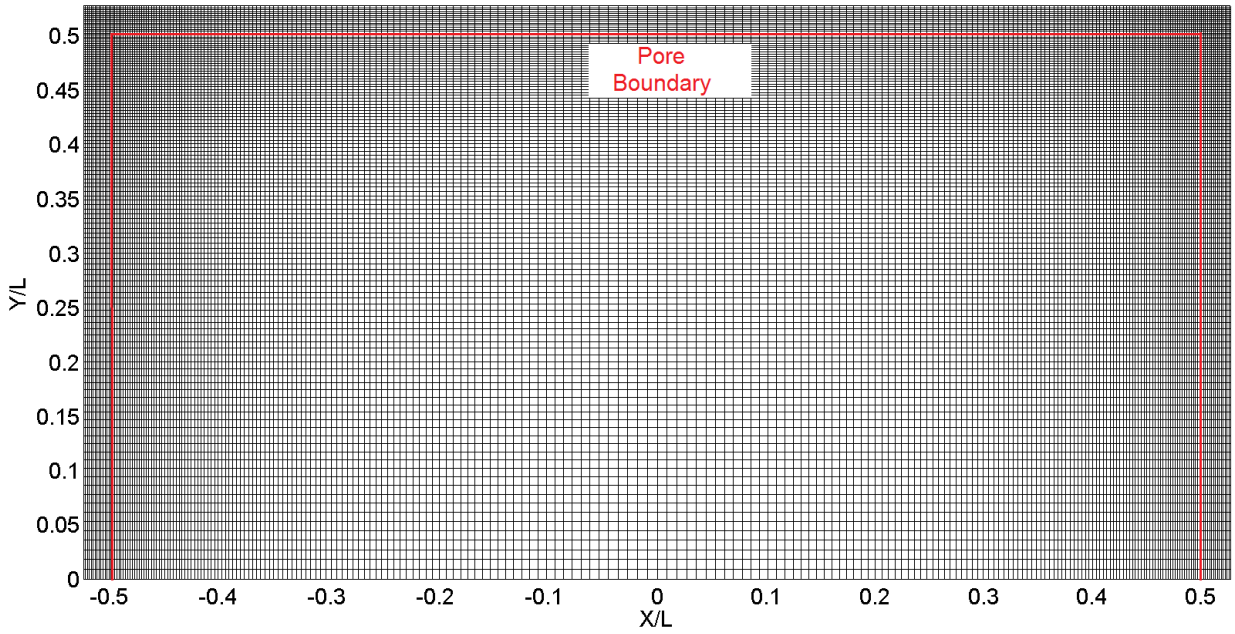

Figure 3.2. Two Dimensional Mesh

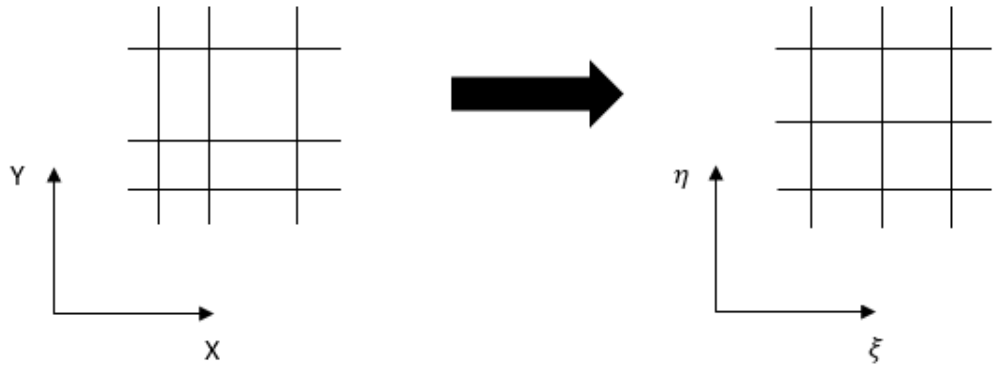

Figure 3.3. Mapping of non-uniform to uniform mesh

The equations are transformed from the x-y co-ordinate system to ξ-η co-ordinate system. There are two forms of the transformation of Laplace equation in generalized co-ordinates: the non-conservative form equation (3.8), and the conservative form equation (3.9). Both forms have advantages and disadvantages. The non-conservative form often requires to calculate derivatives $\nabla^2\xi$ and $\nabla^2\eta$ which are difficult to accurately calculate compared to $x_{\xi\xi}$ and $y_{\eta\eta}$. However, the overall discretization of the non-conservative form is relatively easier than the conservative form.

The governing equation (3.1), equation (3.2) and equation (1.4) are transformed into ξ-η co-ordinate system as follows:

The temperature gradient in ξ-η co-ordinate system is given by:

$$T_x = \frac{1}{J}\left[\left(y_\eta T\right)_\xi - \left(y_\xi T\right)_\eta\right], \tag{3.3}$$

$$T_y = \frac{1}{J}\left[-\left(x_\eta T\right)_\xi + \left(x_\xi T\right)_\eta\right], \tag{3.4}$$

$$J = x_\xi y_\eta - x_\eta y_\xi. \tag{3.5}$$

The non-conservative form of the divergence of gradient is given by:

$$\nabla \cdot \nabla T = \frac{1}{J}\left[\left(y_\eta T_x - x_\eta T_y\right)_\xi + \left(-y_\xi T_x + x_\xi T_y\right)_\eta\right]. \tag{3.6}$$

The non-conservative form of the divergence of gradient is given by:

$$\nabla \cdot \nabla T = \frac{1}{J}\left[y_\eta (T_x)_\xi - x_\eta \left(T_y\right)_\xi - y_\xi (T_x)_\eta + x_\xi \left(T_y\right)_\eta\right]. \tag{3.7}$$

The non-conservative form of transformed Laplace equation is given by:

$$\begin{aligned}\nabla^2 T = \frac{1}{J^2}\left[\left(x_\eta^2 + y_\eta^2\right)T_{\xi\xi} - 2\left(x_\xi x_\eta + y_\xi y_\eta\right)T_{\xi\eta} + \left(x_\xi^2 + y_\xi^2\right)T_{\eta\eta}\right] \\ +\left[\left(\nabla^2 \xi\right)T_\xi + \left(\nabla^2 \eta\right)T_\eta\right].\end{aligned} \tag{3.8}$$

The conservative form of transformed Laplace equation will be:

$$\begin{aligned}J\nabla^2 T = \left\{\frac{1}{J} y_\eta \left[\left(y_\eta T\right)_\xi - \left(y_\xi T\right)_\eta\right] - \frac{1}{J} x_\eta \left[-\left(x_\eta T\right)_\xi + \left(x_\xi T\right)_\eta\right]\right\}_\xi + \\ \left\{-\frac{1}{J} y_\xi \left[\left(y_\eta T\right)_\xi + \left(y_\xi T\right)_\eta\right] + \frac{1}{J} x_\xi \left[-\left(x_\eta T\right)_\xi + \left(x_\xi T\right)_\eta\right]\right\}_\eta.\end{aligned} \tag{3.9}$$

If both co-ordinate systems are parallel to each other, then

$$\mathrm{x}_\eta = 0, \tag{3.10}$$

$$y_\xi = 0. \tag{3.11}$$

Therefore, the non-conservative form of the heat equation (3.7) reduces to:

$$\nabla^2 T = \left[\frac{T_{\xi\xi}}{x_\xi^2} + \frac{T_{\eta\eta}}{y_\eta^2}\right] - \left[\left(\frac{x_{\xi\xi}}{x_\xi^3}\right)T_\xi + \left(\frac{y_{\eta\eta}}{y_\eta^3}\right)T_\eta\right], \tag{3.12}$$

$$T_x = \frac{T_\xi}{x_\xi}, \tag{3.13}$$

$$T_y = \frac{T_\eta}{y_\eta}. \tag{3.14}$$

The equations are transformed from a non-uniform mesh to a mapped uniform mesh. A central finite difference method is used for discretization. The system of equations is solved using explicit iterative scheme. The discretized system of equations is as follows:

$$T_{i,j}^{m+1} = \frac{\left[\left(\frac{T_{i+1,j}^m + T_{i-1,j}^m}{x_\xi^2 \Delta\xi^2}\right) + \left(\frac{T_{i,j+1}^m + T_{i,j-1}^m}{y_\eta^2 \Delta\eta^2}\right)\right]}{2\left(\frac{1}{x_\xi^2 \Delta\xi^2} + \frac{1}{y_\eta^2 \Delta\eta^2}\right)} - \frac{\left[\frac{x_{\xi\xi}}{x_\xi^3}\left(\frac{T_{i+1,j}^m - T_{i-1,j}^m}{2\Delta\xi}\right) + \frac{y_{\eta\eta}}{y_\eta^3}\left(\frac{T_{i,j+1}^m - T_{i,j-1}^m}{2\Delta\eta}\right)\right]}{2\left(\frac{1}{x_\xi^2 \Delta\xi^2} + \frac{1}{y_\eta^2 \Delta\eta^2}\right)}, \tag{3.15}$$

$$x_{\xi\xi} = \frac{x_{i+1,j} - 2x_{i,j} + x_{i-1,j}}{\Delta\xi^2}, \tag{3.16}$$

$$y_{\eta\eta} = \frac{y_{i,j+1} - 2y_{i,j} + y_{i,j-1}}{\Delta\eta^2}, \tag{3.17}$$

$$x_\xi = \frac{x_{i+1,j} - x_{i-1,j}}{2\Delta\xi}, \tag{3.18}$$

$$y_\eta = \frac{y_{i,j+1} + y_{i,j-1}}{2\Delta\eta} \tag{3.19}$$

where the subscript 'i' is the position in ξ direction, subscript 'j' is the position in η direction, superscript 'm' is the iterative step, $\Delta\xi$ and $\Delta\eta$ are the spatial step size.

At the interface, a more complex discretization scheme is required to account for the wall discontinuity. This can be done by balancing the incoming and outgoing heat flux and energy accumulation in conjunction with the temperature jump equation. Figure 3.4 shows discretization scheme at the solid gas interface. The discretized equations at the interface parallel to y axis will be:

$$T_{i+1,j}^{m+1} = \frac{\left(\frac{k_S}{kg}\right)T_{i-1,j}^{m}+\left(\frac{x_{i,j}-x_{i-1,j}}{x_{i+2,j}-x_{i+1,j}}\right)T_{i,j}^{m}+\left(\frac{K_n C L_g \Delta\xi}{x_{i+2,j}-x_{i+1,j}}\right)\left(\frac{k_S}{kg}\right)T_{i+2,j}^{m}}{\left(\frac{x_{i,j}-x_{i-1,j}}{x_{i+2,j}-x_{i+1,j}}\right)+\left(\frac{k_S}{kg}\right)\left[1+\left(\frac{K_n C L_g \Delta\xi}{x_{i+2,j}-x_{i+1,j}}\right)\right]}, \tag{3.20}$$

$$T_{i,j}^{m+1} = \left[1+\left(\frac{K_n C L_g \Delta\xi}{x_{i+2,j}-x_{i+1,j}}\right)\right]T_{i+1,j}^{m+1} - \left(\frac{K_n C L_g \Delta\xi}{x_{i+2}^{j}-x_{i+1}^{j}}\right)T_{i+2,j}^{m+1} \tag{3.21}$$

where the subscript '*i*' is the node located at solid boundary and the subscript '*i+1*' is the node at gas boundary interface.

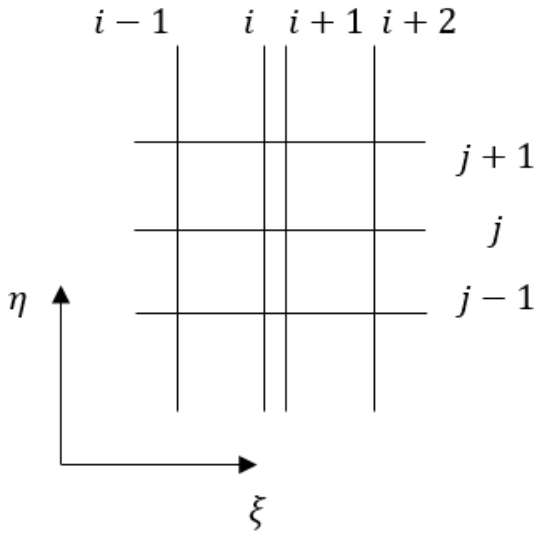

Figure 3.4. Discretization scheme at the solid-gas interface

Similarly, the discretized equations at the interface parallel to x axis are

$$T_{i,j+1}^{m+1} = \frac{\left(\frac{k_S}{k_g}\right)T_{i,j-1}^{m} + \left(\frac{y_{i,j}-y_{i,j-1}}{y_{i,j+2}-y_{i,j+1}}\right)T_{i,j}^{m} + \left(\frac{K_n C L_g \Delta\eta}{y_{i,j+2}-y_{i,j+1}}\right)\left(\frac{k_S}{k_g}\right)T_{i,j+2}^{m}}{\left(\frac{y_{i,j}-y_{i,j-1}}{y_{i,j+2}-y_{i,j+1}}\right) + \left(\frac{k_S}{k_g}\right)\left[1 + \left(\frac{K_n C L_g \Delta\eta}{y_{i,j+2}-y_{i,j+1}}\right)\right]}, \tag{3.22}$$

$$T_{i,j}^{m+1} = \left[1 + \left(\frac{K_n C L_g \Delta\eta}{y_{i,j+2} - y_{i,j+1}}\right)\right] T_{i,j+1}^{m+1} - \left(\frac{K_n C L_g \Delta\eta}{y_{i,j+2} - y_{i,j+1}}\right) T_{i,j+2}^{m+1} \tag{3.23}$$

where '*j*' is the node located at solid boundary and '*j+1*' is the node located at gas boundary interface.

3.4. Physical Properties and Boundary Conditions

This section will present the results of two-dimensional simulations of the porous media for aluminum oxide and air as solid-gas combination. Only steady state cases are considered for this part of study. Additional simulations will also cover the effects of the gases CO_2, H_2 and N_2 with aluminum oxide as solid.

Table 2 of Appendix gives the ideal gas constant *R*, thermal conductivity k_g, viscosity μ, specific heat ratio γ, specific heat c_p, Prandtl number *Pr*, and molecular diameter d_m of the gases used in this investigation (Bird, 1994, Xu, 2003 and Tanak 1998). Table 3 of Appendix shows the density ρ, specific heat c_p, and thermal conductivity *k* of the solid used in this investigation. The solids selected, aluminum oxide, is commonly used as an insulation material. The gases are selected to represent a range of planetary atmospheres: air (Earth), carbon dioxide (Mars and Venus), and hydrogen (Jupiter, Saturn, Uranus, and Neptune). The thermal accommodation coefficient σ_T is considered to be 1 for all the gases throughout in this investigation (Yamaguchi, 2012 and Zhou, 2010).

Initial simulations cover the combination of Al_2O_3 and air to study the effects of the Knudsen number in steady-state cases. The pressure and density of the gases are calculated with the ideal

gas assumption and the mean free path equation (1.2) over the range of the Knudsen number 0 to 0.1. Constant temperature boundary conditions are used at the left and right most boundary surfaces:

$$T\left(x=-\frac{L_s}{2}\right)=T_o, \tag{3.24}$$

$$T\left(x=\frac{L_s}{2}\right)=T_o+\Delta T\,. \tag{3.25}$$

Symmetry boundary conditions are used at the lower and upper boundary surface:

$$\frac{dT}{dy}\left(y=0\right)=0, \tag{3.26}$$

$$\frac{dT}{dy}\left(y=L_s/2\right)=0. \tag{3.27}$$

For the initial simulation, T_o is 280 K, ΔT is 20 K, the pressure and the density corresponds to the Knudsen number in the entire slip flow regime i.e. from 0 to 0.1 and the slot size (L_g) of 100 microns.

3.5. Grid Sensitivity Analysis

A grid sensitivity analysis study is required before further investigation. The single pore model is considered with 90% of cavity volume for this analysis. The mesh density is increased and effective thermal conductivity of the model is computed. The mesh is refined by increasing the number of nodes near the solid-gas interface and change the grid stretching ratio such that the maximum aspect ratio remains below 5. Figure 3.5 shows the effective thermal conductivity with increasing mesh density. Based on the results, a two dimensional mesh with 31626 nodes is considered (see Figure *3.2*).

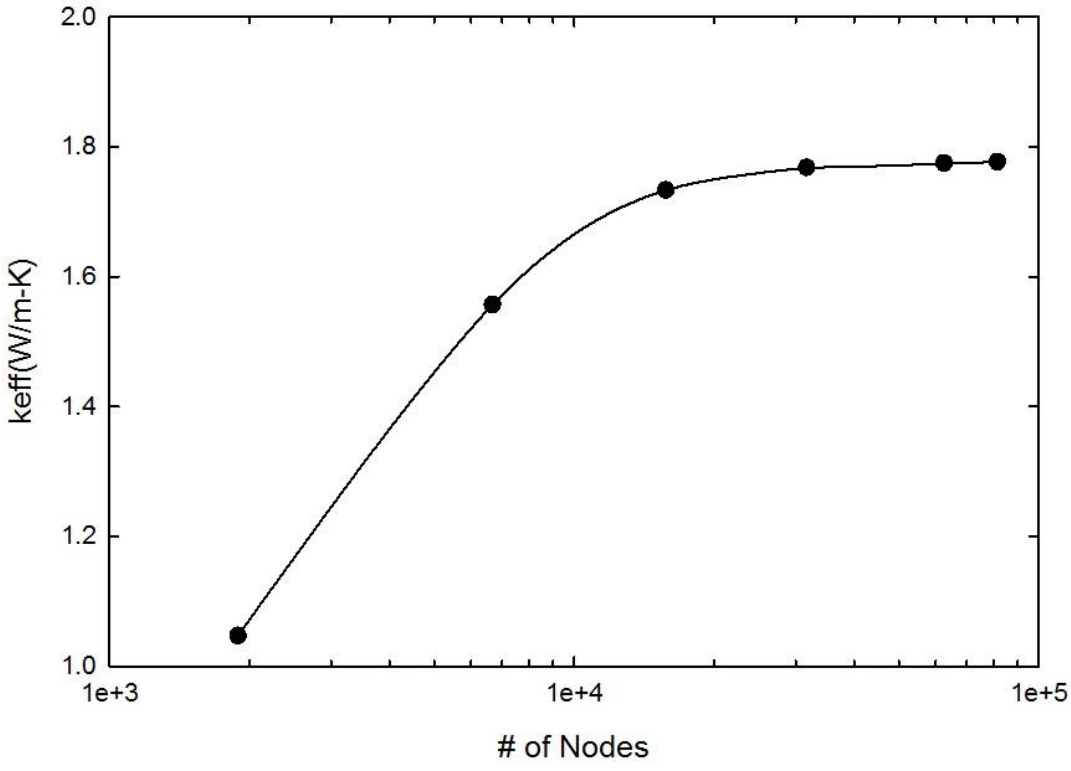

Figure 3.5. Effective thermal conductivity with increasing mesh density

3.6. Void Fraction Analysis

The effective thermal conductivity for the porous model considered in this investigation depends on the thickness *d*, (based on the dimensions given in Figure 3.6) of the solid material which can be correlated to the cavity volume fraction as follows:

$$d = \frac{L_g}{2}\left(\frac{1}{\sqrt{F}} - 1\right) \tag{3.28}$$

where d is the thickness of the solid wall, L_g is the length scale of the cavity, and F is the void fraction.

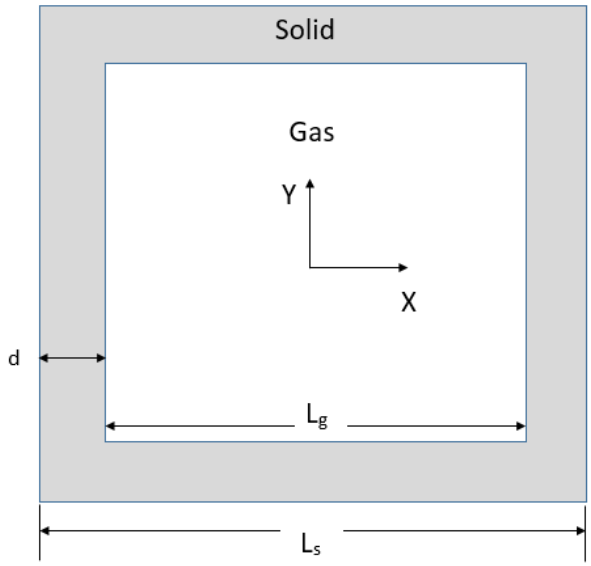

Figure 3.6. Schematic diagram of two-dimensional porous media model

Figure 3.7 shows the effective thermal conductivity of Al_2O_3-air combination with void fraction. The results shows that the effective thermal conductivity reduces significantly as void fraction increases and approaches the thermal conductivity of the air. Insulation material used for heat transfer applications usually have a higher void fraction: greater than 80%. Therefore a void fraction of 0.9 is considered for further investigation.

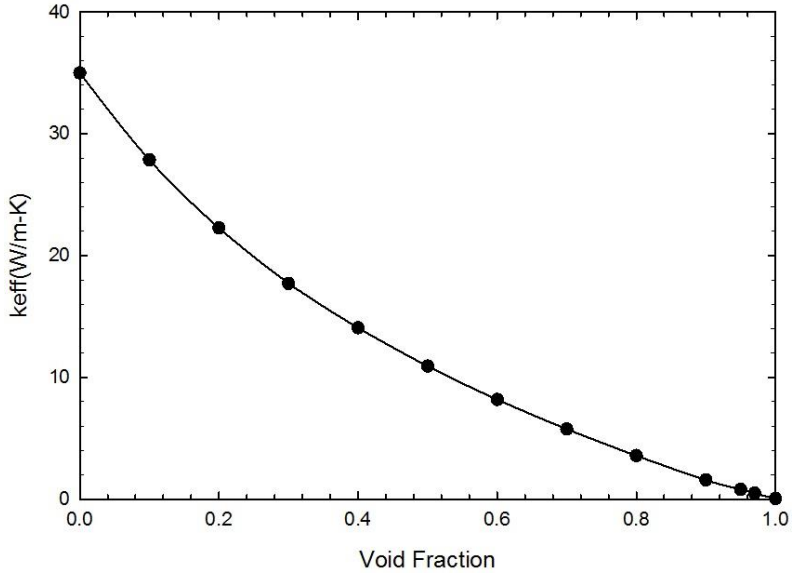

Figure 3.7. Effective thermal conductivity with cavity volume fraction

3.7. Single Pore Model

Figure 3.8 shows the temperature contours of solid and gas of the pore with the cavity length scale of 100 microns and cavity volume as 90% of the total volume at Kn = 0. The solid-gas boundary interface lies at $X/L = \pm 0.5$ and $Y/L = 0.5$. The contour plots shows high temperature gradient and in the gas and very low temperature gradient in the solid due to difference in the thermal conductivity of the materials. However at the interface, the temperature contours are continuous, since this belong to the continuum regime.

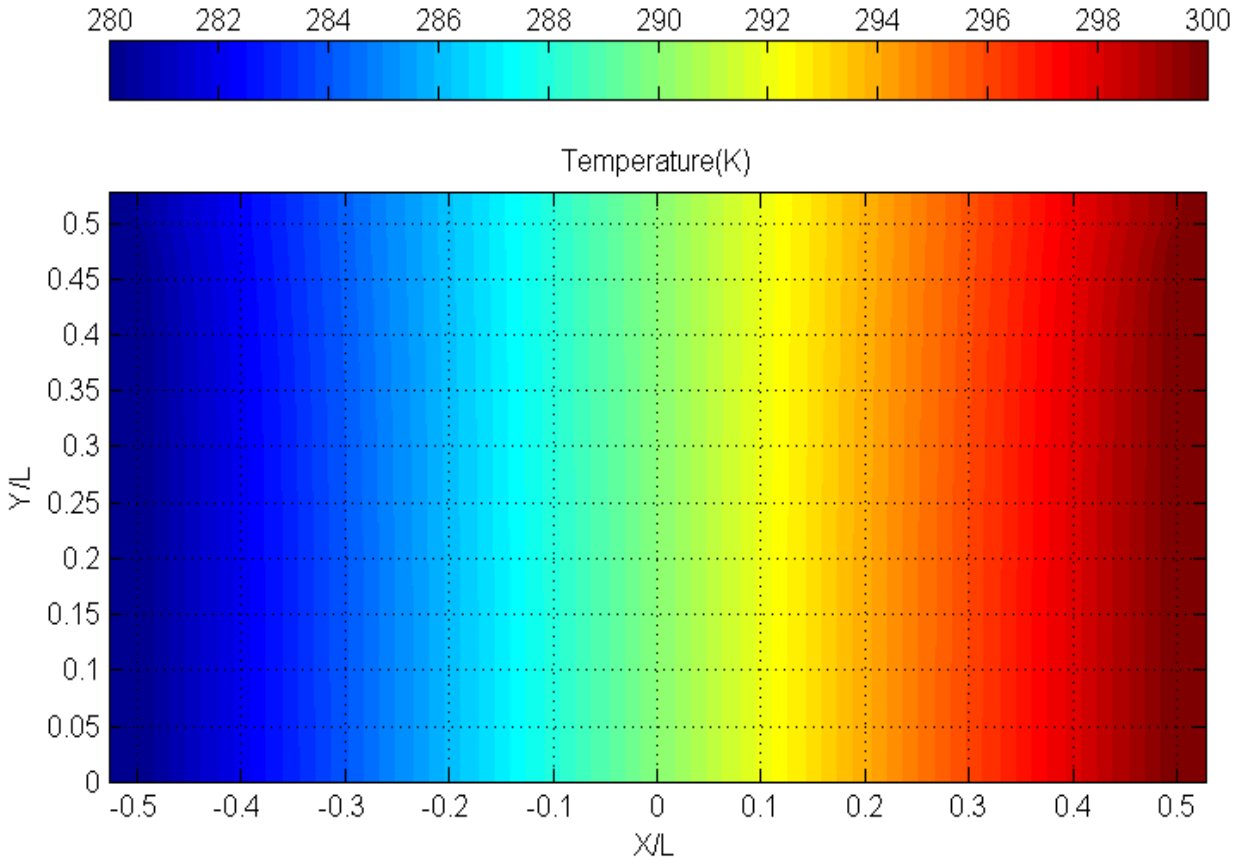

Figure 3.8. Temperature contours at Kn = 0

The simulation is repeated to see the effect of increasing Knudsen number on the temperature contours. Figure 3.9 shows the temperature contour for Kn = 0.1 and it shows that temperature contours changed significantly in gas region. Also, at the solid gas interface the temperature

contours show abrupt change in the temperature across the solid-gas interface because of the temperature jump equation. These effects become noticeable as the Knudsen number increases.

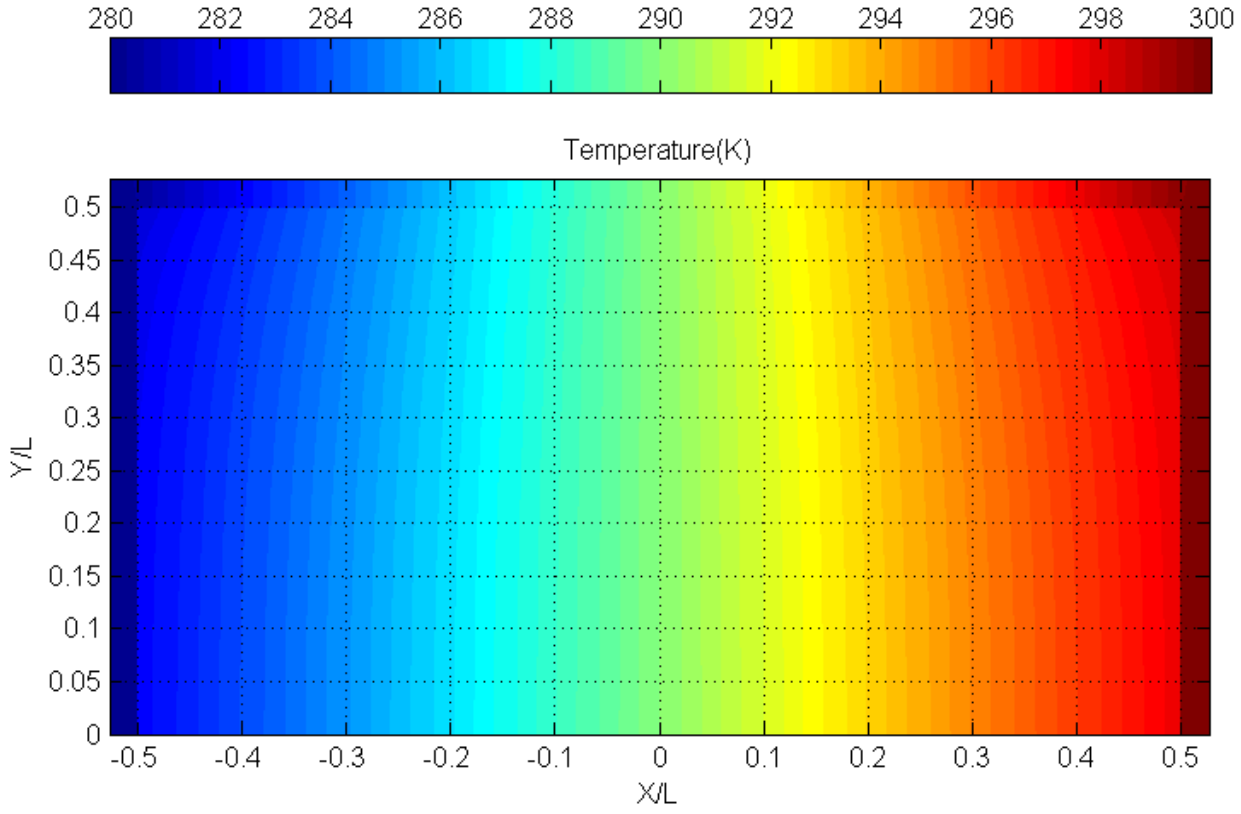

Figure 3.9. Temperature contours at *Kn* = 0.1

The temperature contour plots indicate that there is a temperature jump at the solid gas interface and magnitude of the temperature jump may vary at the location on the solid-gas boundary interface. Therefore, the temperature jump profile on the solid-gas interface is investigated and the effect if the Knudsen number on the magnitude of temperature jump.

Figure 3.10 shows the temperature jump (ΔT) profile at $X/L = 0.5$ for the range of $0 \leq Y/L \leq 0.5$. Since the simulation is performed only for upper half of the model, $Y/L = 0$ is at the center-line and $Y/L = \pm 0.5$ are corners of the solid-gas interface. The temperature jump is maximum at the center and it reduces gradually as we move from center-line towards the corner. Which is because of the edge effect of the pore boundary near the corner where heat flux increases

compared to the center-line of the cavity. The plots also demonstrate the effect of the Knudsen number on temperature jump. The temperature jump is zero at very low Knudsen number in continuum regime and as Knudsen number increase temperature jump condition becomes dominant thus increasing the temperature jump.

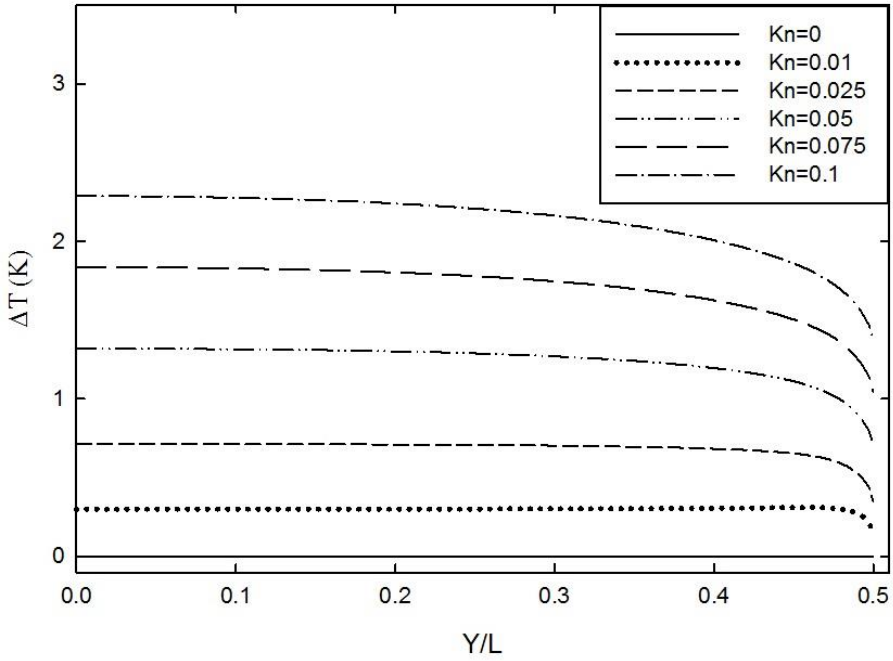

Figure 3.10. Temperature Jump at *X/L* = 0.5

Similarly, the temperature jump profile at the solid-gas interface located at $Y/L = 0.5$ for the range of $-0.5 \leq X/L \leq 0.5$ is also investigated. Figure 3.11 shows the temperature jump along the interface and the effects of the *Kn* on the magnitude of temperature jump. Since this interface is aligned in the direction of heat flow, the temperature is decreasing from one corner to the other corner. Also, since the pore is symmetric around the $Y/L = 0$ line, the magnitude of the temperature jump should be symmetric as well. However since temperature is decreasing along X direction, the solid-gas interface located at $X/L = 0.5$ will have $T_{wall} > T_{gas}$ and the interface at $X/L = -0.5$ will have $T_{wall} < T_{gas}$. Hence, the sign of temperature jump will change which is the reason behind anti-symmetric behavior of temperature jump profile around $Y/L = 0$ line as shown

in the figure below. The Knudsen number also has significant effect on the magnitude of the temperature jump as shown in Figure 3.11.

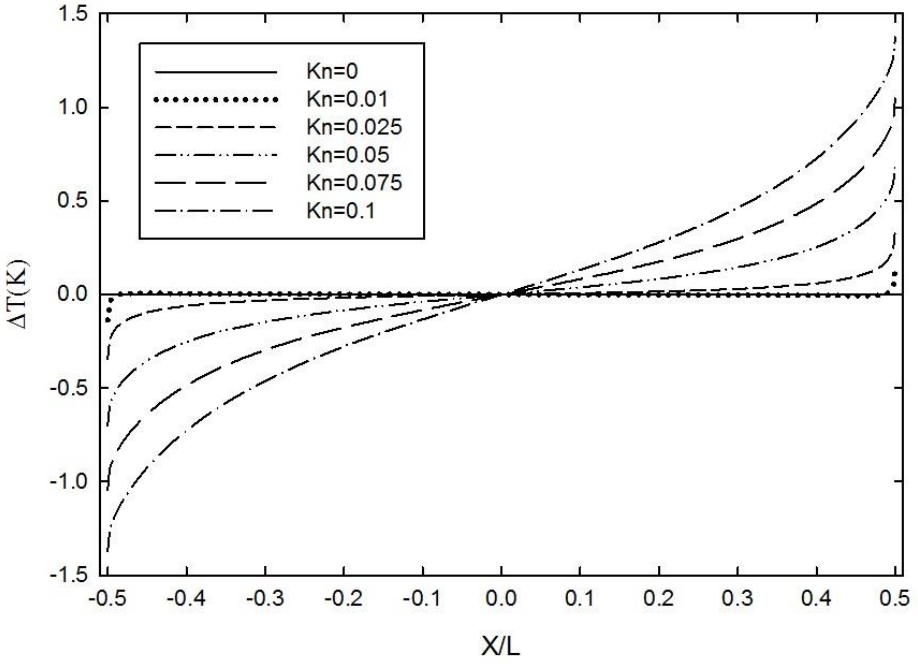

Figure 3.11. Temperature Jump at $Y/L = 0.5$

3.8. Effects of the Gases

As insulations are used in the different environments, the effect of gas properties must be considered. The most abundant gases in our solar system are considered; air (79% N_2 and 21% O_2 by volume), hydrogen (H_2) and carbon dioxide (CO_2) and nitrogen (N_2). These are compared to study the effects on similar parameter as previous cases. Figure 3.12 and Figure 3.13 compares three gases; Air, CO_2 and H_2 for steady state analysis. As shown in the figure, the temperature jump profile changes based on the choice of the gas which is due to different thermal properties of the gases. The temperature jump is lowest for CO_2 and highest for H_2 and Prandtl number is highest for CO_2 and lowest for H_2. This indicates that the temperature jump is inversely proportional of the Prandtl number.

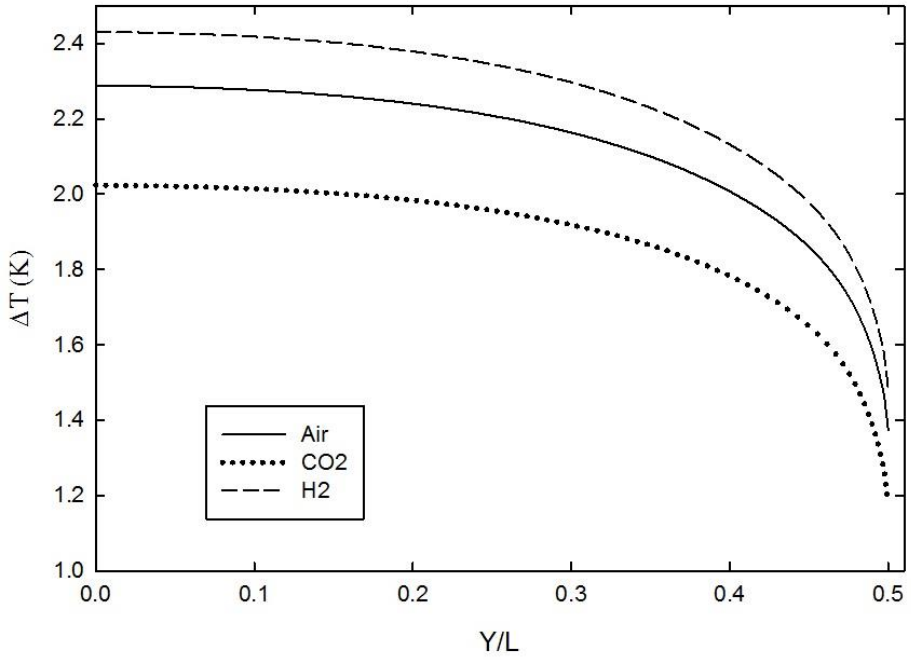

Figure 3.12. Temperature jump profile for different gases at *Y/L* = 0.5 and *Kn* = 0.1

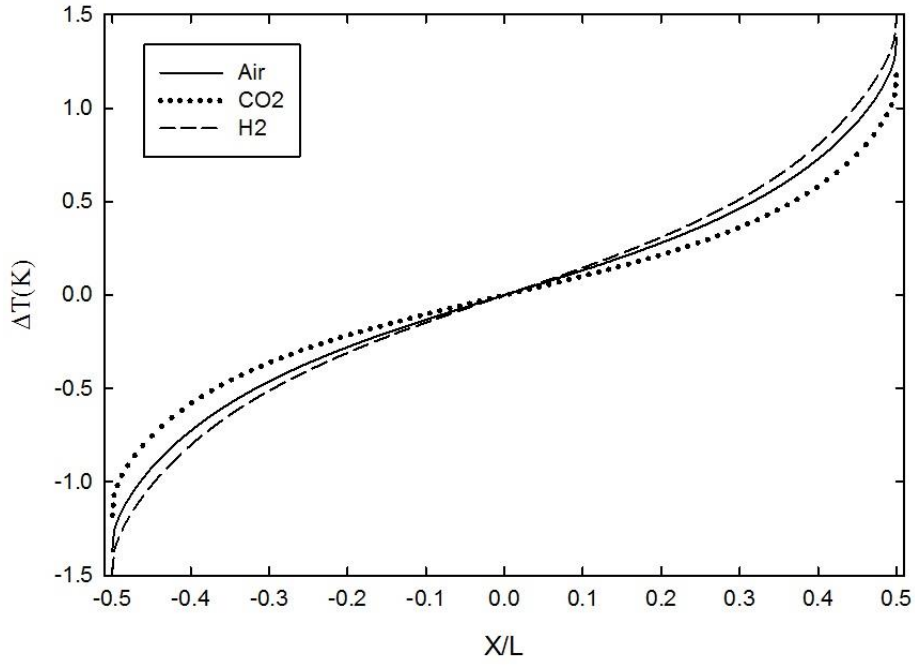

Figure 3.13. Temperature jump profile for different gases at Y/L = 0.5 and *Kn* = 0.1

The effective thermal conductivity of the porous media model is also investigated. Since the gases have different thermal properties, the effective thermal conductivity of the porous media

model will also change. The heat flux profile at the constant temperature boundary ($x=L_s/2$) is calculated using the following equation (3.29) which is further used to calculate the effective thermal conductivity k_{eff} of the model equation (3.30).

$$q''(y) = k_s \frac{dT}{dx}, \tag{3.29}$$

$$k_{eff} = \frac{2\int_0^{\frac{L_S}{2}} q''(y)\, dy}{\Delta T}. \tag{3.30}$$

The effective thermal conductivity is investigated over a range of *Kn* from 10^{-4} to 0.1 and plotted against equivalent pressure in Table 1 of Appendix (see Figure 3.14). The results shows that the effective thermal conductivity decreases at low pressure. The gas also has a significant impact, especially hydrogen because of its very high thermal conductivity and heat capacity. Hence the impact on effective thermal conductivity is larger than air and carbon dioxide.

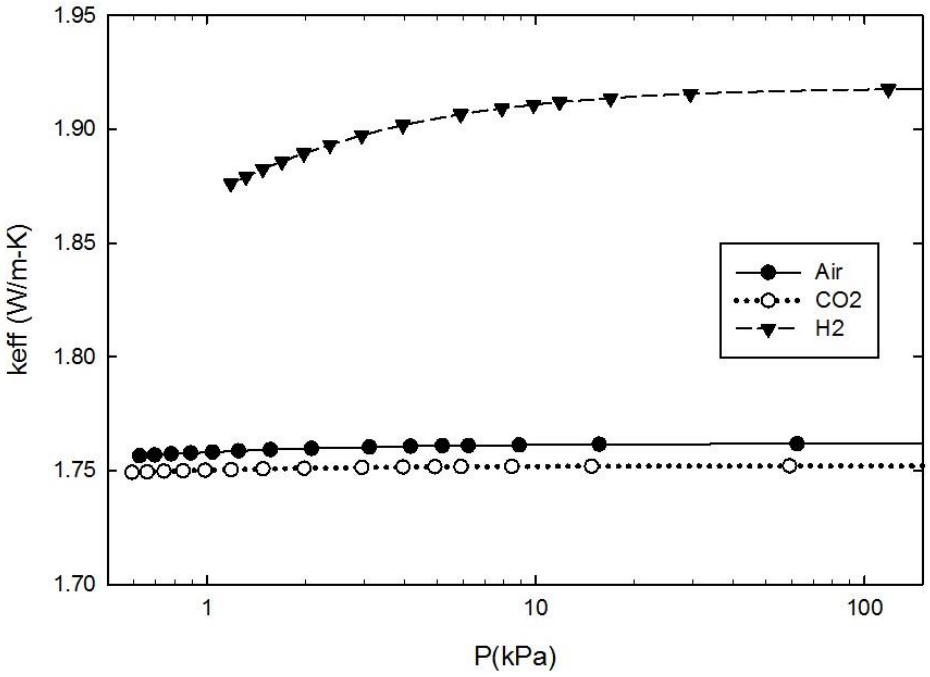

Figure 3.14. Effective thermal conductivity of unit cell for different gases

3.9. Pressure Sensitive Thermal Properties

Previous investigation considered constant thermal properties of the gases. However, the thermal properties of the gases are function of both pressure and temperature. Hence the gases with pressure sensitive thermal properties are also investigated. Table 2 and Table 3 of Appendix represents the thermal properties of CO_2 and N_2 over a range of pressure. The heat flux is computed for entire range of the data presented in the tables, which is used to calculate effective thermal conductivity of the cell with pressure. The results shown in the Figure 3.15 indicates that the k_{eff} is affected by the pressure and the choice of the gas as well. The thermal properties of the gases decreases significantly as pressure decreases and temperature jump condition also becomes dominant at low pressure hence the overall thermal conductivity drop at even higher rate. The results again indicates that the choice of the gas also plays a greater role in the insulation because of the thermal properties. The lower the Prandtl number of the gas, the higher the temperature jump. Thus, decreasing the effective thermal conductivity of the insulation.

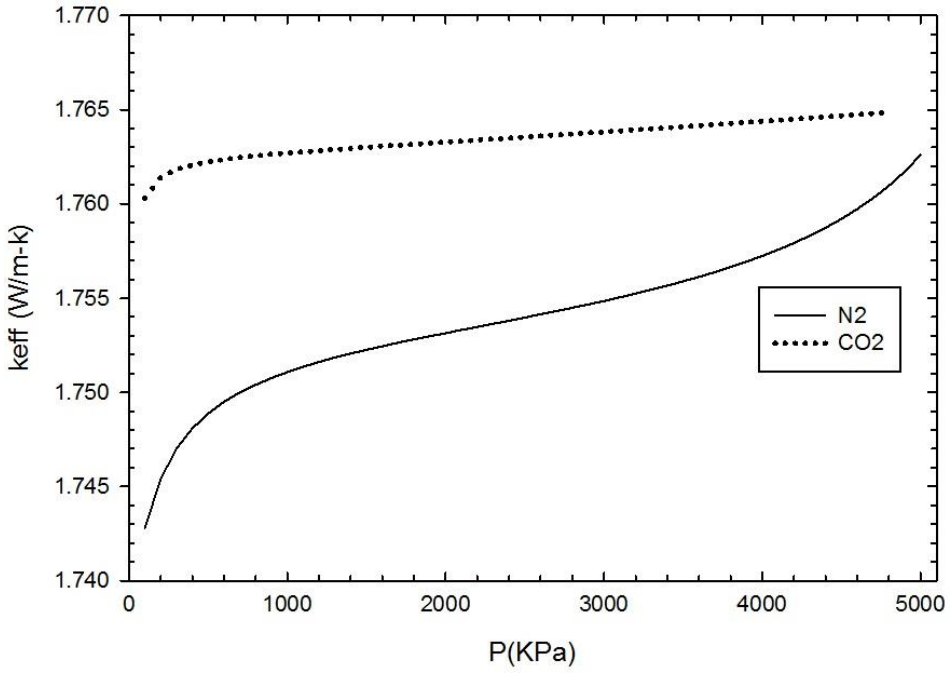

Figure 3.15. Effective thermal conductivity for N_2 and CO_2

3.10. Multiple Pores in Series

Previous sections of this investigation focus on the simulation of a single pore. However in real life applications, the insulation has a finite thickness and multiple layers of the pores stacked over each other which increases the effective thermal resistance of the porous media thus reducing the total heat flow. However, the effective thermal conductivity should be independent of the effective thickness of the insulation layer with the exception of minor edge effects due to consideration of single pore and multiple pore.

Figure 3.16 shows a schematic diagram of three pore models stacked in series. The simulations are performed for multiples pores stacked in the similar fashion. The heat flow is computed to investigate the edge effects on lower number of pores. The number of pores are increased until the effective thermal conductivity became independent of the number of cells considered.

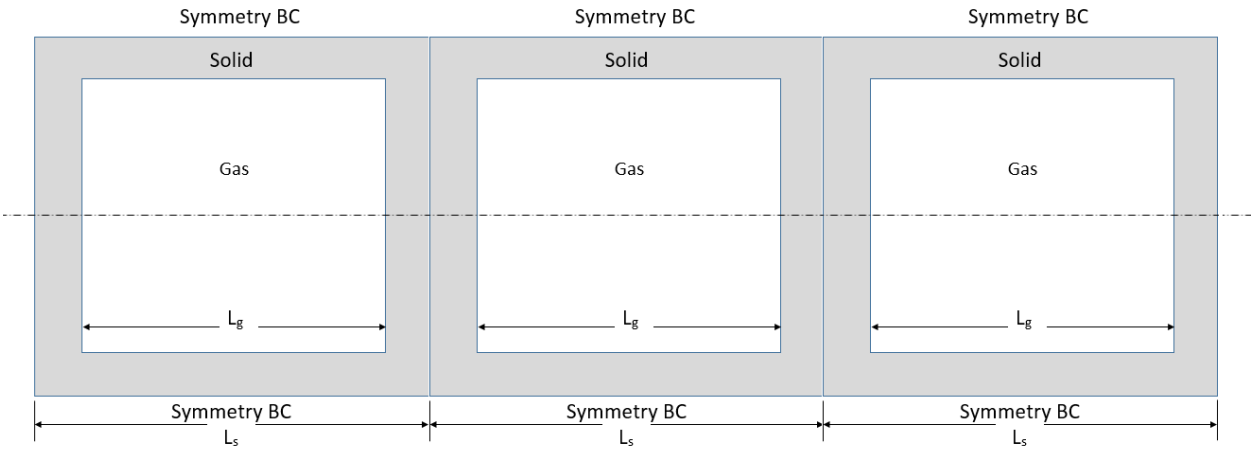

Figure 3.16. Schematic of 3 pores stacked in series

Figure 3.17 presents the effective thermal conductivity with respect to multiple number of pores. Effective thermal conductivity changes with number of cells up to 3 cells due to edge effects. However, after 3 cells, the effective thermal conductivity becomes independent of number of cells considered, which is theoretically true since thermal conductivity is independent of the thickness of the insulation.

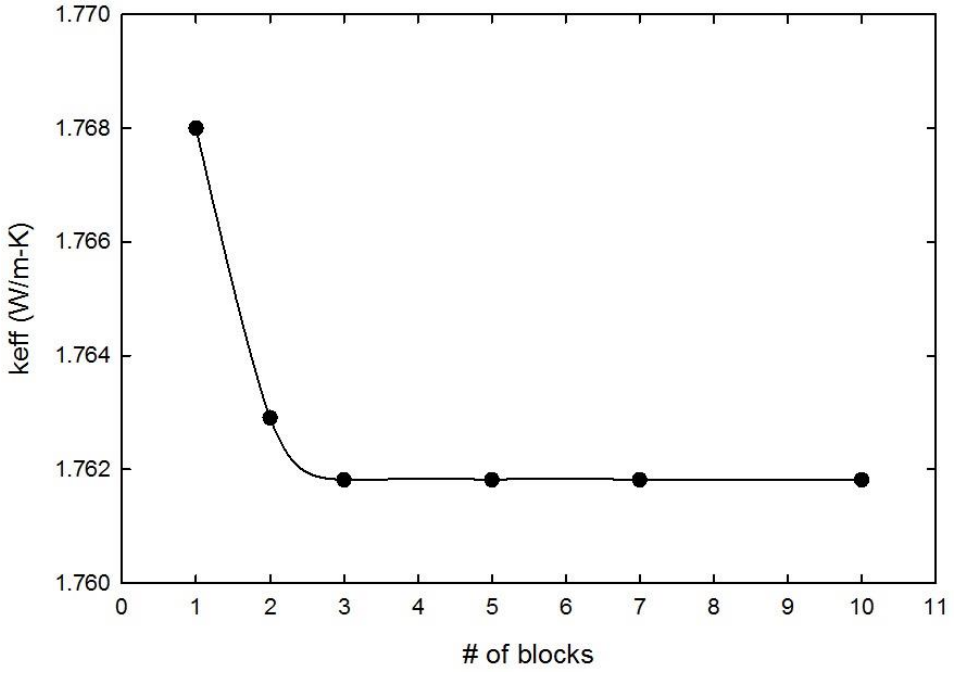

Figure 3.17. Effective thermal conductivity vs thickness of the insulation

3.11. Materials with Very Low Thermal Conductivity

Previous investigation for two-dimensional analysis considered only Al_2O_3 as the solid non-porous material, which has higher thermal conductivity compared to mostly silica based insulation materials. Therefore two silica based most common insulation material (Zircal-18 and Aerogel) are considered for further investigation.

Zircal-18 has ~93% $CaSiO_3$. Therefore, pure $CaSiO_3$ is considered as non-porous material to simulate the thermal behavior of Zircal-18. Thermal conductivity of non-porous $CaSiO_3$ can be calculated using effective thermal conductivity of the mixture CaO+SiO_2 (Wei 2011).

$$k_{CaSiO_3} = \frac{k_{\mathrm{CaO}} + k_{SiO2}}{2}. \tag{3.31}$$

Aerogel is also considered for this investigation. Thermal conductivity of solid aerogel is difficult to quantify. Therefore, an experimental value of k_s for silica-aerogel is used (Wei 2011). Thermal conductivity of non-porous materials is given in the Table 3.1.

Table 3.1. Thermal conductivity of non-porous solid materials

	k (W/m-K)
CaO	1.2511
SiO_2	1.3792
$CaSiO_3$	1.3152
Aerogel	0.25

Figure 3.18 shows the effective thermal conductivity of $CaSiO_3$ and Aerogel with combinations of N_2 and CO_2. The pressure dependent thermal properties of the gases are considered in this case and 3 multiple cells are simulated to remove the edge effects. The results shows extremely low thermal conductivity compared to the previously calculated for Al_2O_3.

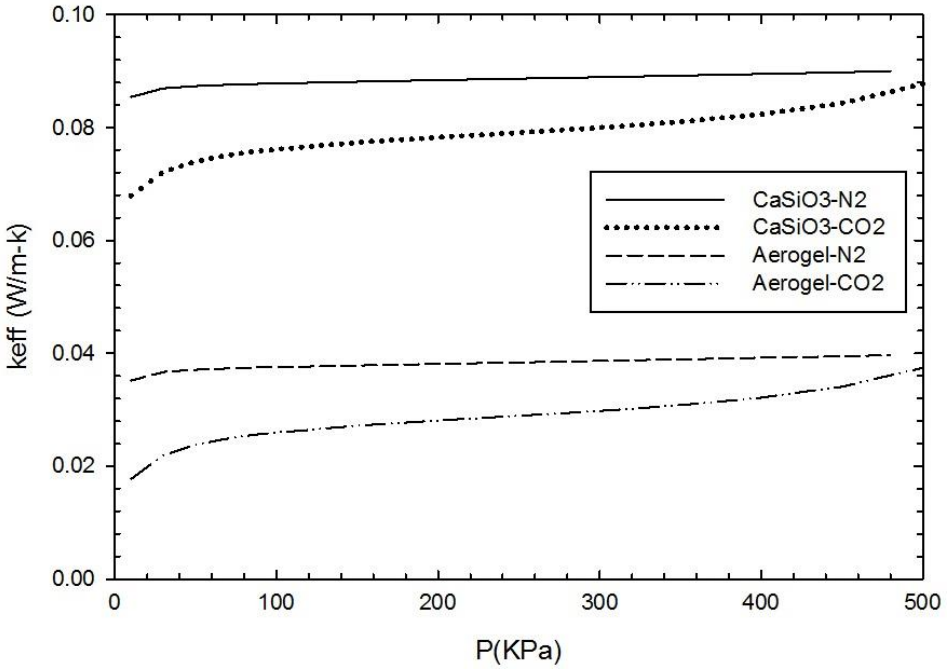

Figure 3.18. Effective thermal conductivity of CaSiO3 and Aerogel with N_2 and CO_2

3.12. Applications

Porous insulations are widely used for their extremely low effective thermal conductivity and low densities. The presence the pores significantly reduces the thermal conductivity by allowing the gas to occupy the cavities. Since gases tends to have very low thermal conductivity, and their thermal properties are both temperature and pressure dependent unlike pure solid materials. Therefore the thermal conductivity of the porous insulations also significantly affected by the pressure and temperature of the environment.

This investigation becomes critical when such insulation materials are used in an environment where pressure changes the thermal behavior of the insulations. One example is application as thermal protection system for spacecraft where insulations layer of the spacecraft is exposed to a hostile environment off different gases. Examples of these environments include gas giants, where hydrogen is available in abundance, or Venus where more than 95% of the atmosphere is carbon dioxide. Since, gases have different thermal properties, their effective thermal properties of the insulation changes based on the ambient gases.

Another application is the deep sea environment where the pressure is extremely high hence the thermal behavior of porous insulations changes due to change in effective thermal conductivity of the insulation. This study focus on low pressure region without mixing of the flow where heat transfer is purely dominated by conduction. However, in some cases of high pressure applications, when there is enough pressure difference to drive the flow across the porous media. This may cause the mixing of the flow and heat transfer is no longer dominated by conduction only. Hence, the mass transport must be considered as well in conjunction with energy equation to study the thermal behavior of porous insulations.

CO_2 sequestration is another important application in the scope of this study. CO_2 sequestration is a process for long term storage of CO_2 to reduce greenhouse effects due to fossil fuel burning. One of the procedure to store CO_2 is to absorb in the porous rocks which changes the thermal resistance of the rock layers. Hence it becomes important to study the heat transfer of the porous rocks to avoid any long term effects.

3.13. Conclusion

A two-dimensional porous media model is investigated with a temperature jump condition obtained from kinetic gas theory after the consideration of slip flow boundary condition at the solid-gas interface in non-continuum region. The temperature jump condition is restricted in the range of $0 < Kn \leq 0.1$. A rectangular pore model is considered for this investigation. The results indicates that the temperature jump at the solid-gas are heavily influenced by the Knudsen number. As the pressure decreases, the Knudsen number increases hence the temperature jump becomes dominant. The temperature jump is also a function of thermal properties and the choice of the gases. The results indicates that the temperature jump is higher for the gases with low Prandtl number. The effects of the pressure sensitive thermal properties are also investigated and the results indicates that the heat flow reduces at low pressure as the thermal properties of the gas are affected. For real life applications, multiple pores are stacked in series to simulate a thick insulation layer of the porous media. The results shows that the thermal conductivity changes due to edge effects at low number of cells. However, it becomes independent of the cells when enough number of cells are considered.

Chapter 4 . Concluding Remarks

The study successfully demonstrates the thermal behavior of porous media at low pressures for one-dimensional and two-dimensional models. The heat equation is solved in conjunction with a temperature jump condition obtained from kinetic gas theory. As previous experimental studies suggested that the effective thermal conductivity of porous media has a pressure dependent behavior, the numerical simulations illustrated the effects of the Knudsen number on effective thermal conductivity of the porous media model.

The one-dimensional steady state and unsteady state analysis is performed with a one-dimensional slot model of the order of 100 micrometers. The results indicates that the solid-gas interfaces have a temperature jump at low pressures when the Knudsen number is higher than 0.001. This corresponds to the slip flow regime. The heat flux of the porous media is also affected by the temperature jump condition. As the pressure decreases, the Knudsen number increases and the temperature jump condition becomes significant. This increases the effective thermal resistance of the model this reducing the overall heat transfer. The effects are more noticeable as lower pressure or at higher Knudsen number.

The one-dimensional porous media model is also investigated for unsteady state with a step boundary condition and periodic boundary condition. The results illustrated that the heat flux and phase difference are directly affected by the Knudsen number of the gas present in the slot, frequency of the periodic boundary condition, and size of the slot relative to the solid. The analysis further continued out to study the effects of the solids (aluminum oxide and titanium) and gases (air, hydrogen, and carbon dioxide). The results shows that the choice of the gas has a significant impact of the temperature jump and heat flux. However, the solids have an insignificant effect.

The study is further continued on a two-dimensional rectangular porous media model with a length scale of the cavity of the order and 100 micrometers and 90% of the total volume of a unit cell. The steady state analysis produced the temperature jump profile at the solid-gas interface along the periphery of the cavity. The effect of the low pressure is seen in the temperature jump profile, as well as the effective thermal conductivity of the model. The results indicates that the effective thermal conductivity of the unit cell reduces as pressure of the gas present in the cavity reduces. The effect of the gas on the effective thermal conductivity is also studied for different gases (air, hydrogen, carbon dioxide, and nitrogen). The effective thermal conductivity of the unit cell depends on the gas because of the difference in their thermal properties of the gas.

The analysis is further extended for multi-cell structures to simulate an insulation layer with a finite thickness. The unit cells are stacked in series to increase the overall thickness of the insulation layer. The results shows that the effective thermal conductivity of the layer reduces due to edge effects for lower number of cells. However it becomes independent of the cells numbers after enough number of cells are considered, as in theory thermal conductivity is independent of the thickness of the insulation layer.

References

Basilevsky, A. T., Invanov , M. A., Head J. W., Aittola, M., and Raitala, J., “Landing on Venus: Past and Future,” Planetary and Space Science 55 2097, 2007.

Bird, G. A., “Molecular Gas Dynamics and the Simulation of Gas Flows”, Oxford, U.K.: Clarendon, 1994.

Druma, A.M., Alam, M.K., Druma C., “Analysis of thermal conduction in carbon foams”, International Journal of Thermal Sciences, Vol. 43, Issue 7, pp. 689–695, 2004.

Du N., Fan J., and Wu, H., “Optimum Porosity of Fibrous Porous Materials for Thermal Insulation”, Fibers and Polymers, Vol. 9, Issue 1, pp 27-33, 2008.

Firouzi, M.and Wilcox, J., "Slippage and viscosity predictions in carbon micropores and their influence on CO2 and CH4 transport", The Journal of Chemical Physics, 138, 064705, 2013.

Fletcher, C. A. J., Computational Techniques for Fluid Dynamics. Springer Series in Computation Physics, 1991.

Gunter, W. D., Perkins, E. H., McCann, T. J., “Aquifer disposal of CO2-rich gases: Reaction design for added capacity”, Energy Conversion and Management, Vol. 34, Issues 9–11, September–November 1993, Pages 941-948.

Jaluria, Y. and Torrance, K.E., “Computational Heat Transfer”,CRC Press 2002.

Litosky, E. Y. and Shapiro, M., “Gas Pressure and Dependences of Thermal Conductivity of Porous Ceramic Materials: Part 1, Refractories and Ceramics with Porosity below 30%,” Journal of the American Ceramics Society, 75 3425, 1992.

Litovsky, E. Y. and Shapiro, M., and Shavit, A. “Gas Pressure and Dependences of Thermal Conductivity of Porous Ceramic Materials: Part 1, Refractories and Ceramics with Porosity Exceeding 30%,” Journal of the American Ceramics Society, 79 1366, 1996.

Nutsugah, R., Triay, M., Cooley, A., Sparacino, D., LaCour, T., Castillo, J., Maynard, D., Akwaboa, S., Martin, M. J., Mensah, P. F., and Pauken, M., Design, Integration, and Initial Testing of an Integrated System for Thermal Conductivity Measurement of Insulation Materials at High Pressure,” Proceedings, AIAA Science and Technology Forum and Exposition (SciTech2014), Washington, DC, 2014.

Ozisik, N., Finite Difference Methods in Heat Transfer. CRC Press Inc., 1994

Park, J. H., Baek, S. W., Kang, S. J. and Yu, M. J., “Analysis Of Thermal Slip In Oscillating Rarefied Flow Using DSMC”, Numerical Heat Transfer, Vol. 42, Issue 6, 2002.

Pauken, M., Li, L., Almasco, D., Castillo, L. D., Luvender M. V., Beatty, J., Knopp, M., and Polk, J., “Insulation Materials development for Potential Venus Surface Missions,” AIAA Paper 2011-256, 2011.

Petrov, V. A., “Combined radiation and conduction heat transfer in high temperature fiber thermal insulation”, International Journal of Heat and Mass Transfer, Vol. 40, No. 9, pp. 2241-2247, 1997.

Smoluchowski, M. Smolan V., “Über Wärmeleitung in Verdünnten Gasen,” Annalen der Physik und Chemie, 300 101, 1898.

Tanaka, H., Ishikawa, T., Masai, T., Sagara , T., Boesten, L., Takekawa, M., Itikawa, Y., and Kimura, M., “Elastic collisions of low- to intermediate-energy electrons from carbon dioxide: Experimental and theoretical differential cross sections”, Physics Review A 57, 1998.

Wei, G., Liu Y., Zhang, X., Yu F., Du X., “Thermal Conductivity study on silica aerogeland its composite insulation materials”, International Journal of Heat and Mass Transfer 54, 2355-2366 (2011).

Woodside, W. and Messmer, J. H., “Thermal Conductivity of Porous Media. I. Unconsolidated Sands”, Journal of Applied Physics 32, 1688 (1961).

Xu, X., Yang, W., Song, C., Liu, J., and Lin, L., “Hydrogen Separation by Zeolite Membranes”, Fuel Chemistry Division Preprints, 48(1), 284-285, 2003

Yamaguchi, H., Kanazawa, K., Yu M., Niimi, T., Polikarpov, A., and Graur I., “Investigation on heat transfer between two coaxial cylinders for measurement of thermal accommodation coefficient”, Phycics of Fluids, 24, 062002, 2012.

Zheng, G., Verret, A., Burke, N., Prescott, N., Cai, D., and Perera, R., “An Update on Heat Transfer in a Porous Insulation Medium in a Subsea Bundled Pipeline,” Journal of Energy Resources Technology, Vol. 123, pp, 285-290, 2001.

Zhou, W., Liu, B., Yu, S., and Hua, W., “Numerical Simulations of Accommodation Coefficient Effects at the Head-Disk Interface”, Japanese Journal of Applied Physics, 49, 095206, 2010.

Appendix: Thermal Properties of Gases

Table 1. Pressure vs Knudsen number for gases used

Kn	$P_{CO_2}(Pa)$	$P_{H_2}(Pa)$	$P_{Air}(Pa)$
0.01	4185	10790	5133
0.02	2092	5395	2566
0.03	1395	3597	1711
0.04	1046	2697	1283
0.05	837	2158	1026
0.06	697	1798	855
0.07	598	1541	733
0.08	523	1349	641
0.09	465	1199	570
0.1	418	1079	513

Table 2. Pressure sensitive thermal properties of CO_2

Temperature (K)	Pressure (MPa)	Density (kg/m3)	Cv (J/g*K)	Cp (J/g*K)	Viscosity (Pa*s)	Therm. Cond. (W/m*K)	ni (m-3)	lambda (m)
290	0.1	1.8352	0.64922	0.84293	1.45E-05	0.01599	2.5E+25	8.5E-08
290	0.2	3.6909	0.65203	0.8507	1.45E-05	0.01604	5E+25	4.2E-08
290	0.3	5.5675	0.65488	0.85869	1.46E-05	0.01609	7.6E+25	2.8E-08
290	0.4	7.4658	0.65778	0.86691	1.46E-05	0.01614	1E+26	2.1E-08
290	0.5	9.3864	0.66071	0.87537	1.46E-05	0.01619	1.3E+26	1.7E-08
290	0.6	11.33	0.66369	0.88407	1.46E-05	0.01624	1.5E+26	1.4E-08
290	0.7	13.297	0.66671	0.89305	1.46E-05	0.0163	1.8E+26	1.2E-08
290	0.8	15.289	0.66978	0.90231	1.46E-05	0.01635	2.1E+26	1E-08
290	0.9	17.306	0.67289	0.91186	1.46E-05	0.01641	2.4E+26	9E-09
290	1	19.349	0.67607	0.92172	1.46E-05	0.01647	2.6E+26	8E-09

(Table 2 continued)

Temperature (K)	Pressure (MPa)	Density (kg/m3)	Cv (J/g*K)	Cp (J/g*K)	Viscosity (Pa*s)	Therm. Cond. (W/m*K)	ni (m-3)	lambda (m)
290	1.1	21.419	0.67929	0.93192	1.46E-05	0.01654	2.9E+26	7.3E-09
290	1.2	23.517	0.68258	0.94247	1.47E-05	0.0166	3.2E+26	6.6E-09
290	1.3	25.644	0.68592	0.9534	1.47E-05	0.01667	3.5E+26	6.1E-09
290	1.4	27.801	0.68933	0.96472	1.47E-05	0.01674	3.8E+26	5.6E-09
290	1.5	29.989	0.69281	0.97646	1.47E-05	0.01681	4.1E+26	5.2E-09
290	1.6	32.209	0.69636	0.98865	1.47E-05	0.01689	4.4E+26	4.8E-09
290	1.7	34.463	0.69998	1.0013	1.48E-05	0.01697	4.7E+26	4.5E-09
290	1.8	36.751	0.70368	1.0145	1.48E-05	0.01705	5E+26	4.2E-09
290	1.9	39.076	0.70747	1.0282	1.48E-05	0.01714	5.3E+26	4E-09
290	2	41.438	0.71135	1.0425	1.48E-05	0.01723	5.7E+26	3.7E-09
290	2.1	43.84	0.71532	1.0575	1.48E-05	0.01732	6E+26	3.5E-09
290	2.2	46.284	0.71939	1.0731	1.49E-05	0.01742	6.3E+26	3.4E-09
290	2.3	48.77	0.72357	1.0894	1.49E-05	0.01752	6.7E+26	3.2E-09
290	2.4	51.301	0.72786	1.1066	1.49E-05	0.01763	7E+26	3E-09
290	2.5	53.879	0.73227	1.1246	1.50E-05	0.01774	7.4E+26	2.9E-09
290	2.6	56.507	0.73681	1.1435	1.50E-05	0.01786	7.7E+26	2.7E-09
290	2.7	59.187	0.74149	1.1633	1.50E-05	0.01798	8.1E+26	2.6E-09
290	2.8	61.922	0.74632	1.1843	1.51E-05	0.01811	8.5E+26	2.5E-09
290	2.9	64.715	0.7513	1.2065	1.51E-05	0.01825	8.9E+26	2.4E-09
290	3	67.568	0.75645	1.23	1.51E-05	0.01839	9.2E+26	2.3E-09
290	3.1	70.487	0.76179	1.2549	1.52E-05	0.01855	9.6E+26	2.2E-09
290	3.2	73.474	0.76733	1.2814	1.52E-05	0.01871	1E+27	2.1E-09
290	3.3	76.533	0.77307	1.3097	1.53E-05	0.01888	1E+27	2E-09
290	3.4	79.671	0.77906	1.3399	1.53E-05	0.01906	1.1E+27	2E-09
290	3.5	82.891	0.7853	1.3723	1.54E-05	0.01926	1.1E+27	1.9E-09
290	3.6	86.2	0.79181	1.4071	1.54E-05	0.01947	1.2E+27	1.8E-09

(Table 2 continued)

Temperature (K)	Pressure (MPa)	Density (kg/m3)	Cv (J/g*K)	Cp (J/g*K)	Viscosity (Pa*s)	Therm. Cond. (W/m*K)	ni (m-3)	lambda (m)
290	3.7	89.605	0.79863	1.4447	1.55E-05	0.01969	1.2E+27	1.7E-09
290	3.8	93.113	0.8058	1.4854	1.55E-05	0.01993	1.3E+27	1.7E-09
290	3.9	96.732	0.81333	1.5297	1.56E-05	0.02019	1.3E+27	1.6E-09
290	4	100.47	0.82129	1.578	1.57E-05	0.02047	1.4E+27	1.5E-09
290	4.1	104.35	0.82971	1.6312	1.57E-05	0.02078	1.4E+27	1.5E-09
290	4.2	108.36	0.83866	1.6899	1.58E-05	0.02111	1.5E+27	1.4E-09
290	4.3	112.54	0.84822	1.7552	1.59E-05	0.02148	1.5E+27	1.4E-09
290	4.4	116.9	0.85846	1.8283	1.60E-05	0.02188	1.6E+27	1.3E-09
290	4.5	121.46	0.86951	1.9109	1.61E-05	0.02232	1.7E+27	1.3E-09
290	4.6	126.24	0.88149	2.0052	1.62E-05	0.02282	1.7E+27	1.2E-09
290	4.7	131.28	0.89459	2.1141	1.63E-05	0.02338	1.8E+27	1.2E-09
290	4.8	136.62	0.90903	2.2416	1.64E-05	0.02402	1.9E+27	1.1E-09
290	4.9	142.31	0.92513	2.3934	1.66E-05	0.02475	1.9E+27	1.1E-09

Table 3: Pressure sensitive thermal properties of N_2

Pressure (MPa)	Density (kg/m3)	Cv (J/g*K)	Cp (J/g*K)	Viscosity (Pa*s)	Therm. Cond. (W/m*K)	ni (m-3)	lambda (m)
0.1	1.1621	20.815	29.171	1.74E-05	0.025185	2.499E+25	9.057E-08
0.2	2.3248	20.822	29.22	1.74E-05	0.025217	5E+25	4.527E-08
0.3	3.4882	20.83	29.269	1.75E-05	0.02525	7.502E+25	3.017E-08
0.4	4.6521	20.838	29.318	1.75E-05	0.025284	1E+26	2.263E-08
0.5	5.8166	20.845	29.368	1.75E-05	0.025319	1.251E+26	1.81E-08
0.6	6.9816	20.853	29.417	1.75E-05	0.025355	1.501E+26	1.508E-08
0.7	8.1471	20.86	29.466	1.75E-05	0.025391	1.752E+26	1.292E-08
0.8	9.3132	20.868	29.516	1.75E-05	0.025429	2.003E+26	1.13E-08

(Table 3 continued)

Pressure (MPa)	Density (kg/m3)	Cv (J/g*K)	Cp (J/g*K)	Viscosity (Pa*s)	Therm. Cond. (W/m*K)	ni (m-3)	lambda (m)
0.9	10.48	20.875	29.565	1.76E-05	0.025467	2.254E+26	1.004E-08
1	11.647	20.882	29.615	1.76E-05	0.025506	2.505E+26	9.037E-09
1.1	12.814	20.89	29.664	1.76E-05	0.025546	2.756E+26	8.214E-09
1.2	13.982	20.897	29.714	1.76E-05	0.025586	3.007E+26	7.528E-09
1.3	15.151	20.905	29.763	1.76E-05	0.025627	3.258E+26	6.947E-09
1.4	16.32	20.912	29.813	1.77E-05	0.025669	3.51E+26	6.449E-09
1.5	17.489	20.919	29.862	1.77E-05	0.025712	3.761E+26	6.018E-09
1.6	18.658	20.927	29.912	1.77E-05	0.025755	4.012E+26	5.641E-09
1.7	19.828	20.934	29.961	1.77E-05	0.025799	4.264E+26	5.308E-09
1.8	20.999	20.941	30.011	1.77E-05	0.025844	4.516E+26	5.012E-09
1.9	22.169	20.949	30.061	1.77E-05	0.025889	4.768E+26	4.748E-09
2	23.34	20.956	30.11	1.78E-05	0.025935	5.019E+26	4.51E-09
2.1	24.511	20.963	30.16	1.78E-05	0.025982	5.271E+26	4.294E-09
2.2	25.683	20.97	30.209	1.78E-05	0.026029	5.523E+26	4.098E-09
2.3	26.854	20.978	30.259	1.78E-05	0.026076	5.775E+26	3.92E-09
2.4	28.026	20.985	30.309	1.78E-05	0.026125	6.027E+26	3.756E-09
2.5	29.199	20.992	30.358	1.78E-05	0.026174	6.279E+26	3.605E-09
2.6	30.371	20.999	30.408	1.79E-05	0.026223	6.531E+26	3.466E-09
2.7	31.544	21.006	30.458	1.79E-05	0.026273	6.784E+26	3.337E-09
2.8	32.716	21.013	30.507	1.79E-05	0.026323	7.036E+26	3.217E-09
2.9	33.889	21.02	30.557	1.79E-05	0.026374	7.288E+26	3.106E-09
3	35.062	21.027	30.606	1.79E-05	0.026426	7.54E+26	3.002E-09
3.1	36.235	21.034	30.656	1.80E-05	0.026478	7.792E+26	2.905E-09
3.2	37.409	21.042	30.706	1.80E-05	0.02653	8.045E+26	2.814E-09
3.3	38.582	21.049	30.755	1.80E-05	0.026583	8.297E+26	2.728E-09
3.4	39.755	21.056	30.805	1.80E-05	0.026636	8.549E+26	2.648E-09

(Table 3 continued)

Pressure (MPa)	Density (kg/m3)	Cv (J/g*K)	Cp (J/g*K)	Viscosity (Pa*s)	Therm. Cond. (W/m*K)	ni (m-3)	lambda (m)
3.4	39.755	21.056	30.805	1.80E-05	0.026636	8.549E+26	2.648E-09
3.4	39.755	21.056	30.805	1.80E-05	0.026636	8.549E+26	2.648E-09
3.5	40.928	21.063	30.854	1.80E-05	0.02669	8.802E+26	2.572E-09
3.6	42.102	21.069	30.904	1.81E-05	0.026744	9.054E+26	2.5E-09
3.7	43.275	21.076	30.953	1.81E-05	0.026798	9.306E+26	2.432E-09
3.8	44.449	21.083	31.002	1.81E-05	0.026853	9.559E+26	2.368E-09
3.9	45.622	21.09	31.052	1.81E-05	0.026909	9.811E+26	2.307E-09
4	46.795	21.097	31.101	1.81E-05	0.026964	1.006E+27	2.249E-09
4.1	47.968	21.104	31.15	1.82E-05	0.02702	1.032E+27	2.194E-09
4.2	49.141	21.111	31.199	1.82E-05	0.027077	1.057E+27	2.142E-09
4.3	50.314	21.118	31.249	1.82E-05	0.027134	1.082E+27	2.092E-09
4.4	51.487	21.124	31.298	1.82E-05	0.027191	1.107E+27	2.044E-09
4.5	52.66	21.131	31.347	1.82E-05	0.027248	1.132E+27	1.999E-09
4.6	53.832	21.138	31.396	1.83E-05	0.027306	1.158E+27	1.955E-09
4.7	55.004	21.145	31.445	1.83E-05	0.027364	1.183E+27	1.914E-09
4.8	56.176	21.151	31.494	1.83E-05	0.027422	1.208E+27	1.874E-09

Vita

Pravin Kumar was born and raised in Bhatasa, Uttar Pradesh, India. After finishing higher secondary education he attended Indian Institute of Technology, Kanpur where he received his Bachelor of Technology degree in Aerospace Engineering in 2009. Between 2009 and 2012 he worked at Sener, Madrid, Spain. To further his knowledge in the field of science and technology, he enrolled in the Department of Mechanical and Industrial Engineering at Louisiana State University (LSU) in Spring 2013. He expects to graduate in December of 2015.